


Ocean atmosphere thermal decoupling in the eastern equatorial Indian ocean

Sudheer Joseph¹  · M. Ravichandran¹ · B. Praveen Kumar¹ · Raju V. Jampana¹ · Weiqing Han²

Received: 2 March 2016 / Accepted: 8 September 2016 / Published online: 22 September 2016
© Springer-Verlag Berlin Heidelberg 2016

Abstract Eastern equatorial Indian ocean (EEIO) is one of the most climatically sensitive regions in the global ocean, which plays a vital role in modulating Indian ocean dipole (IOD) and El Niño southern oscillation (ENSO). Here we present evidences for a paradoxical and perpetual lower co-variability between sea-surface temperature (SST) and air-temperature (T_{air}) indicating instantaneous thermal decoupling in the same region, where signals of the strongly coupled variability of SST anomalies and zonal winds associated with IOD originate at inter-annual time scale. The correlation minimum between anomalies of T_{air} and SST occurs in the eastern equatorial Indian ocean warm pool region ($\approx 70^{\circ}\text{E}$ – 100°E , 5°S – 5°N), associated with lower wind speeds and lower sensible heat fluxes. At sub-monthly and Madden–Julian oscillation time scales, correlation of both variables becomes very low. In above frequencies, precipitation positively contributes to the low correlation by dropping T_{air} considerably while leaving SST without any substantial instant impact. Precipitation is led by positive build up of SST and post-facto drop in it. The strong semi-annual response of SST to mixed layer variability and equatorial waves, with the absence of the same in the T_{air} , contributes further to the weak correlation at the sub-annual scale. The limited correlation found in the EEIO is mainly related to the annual warming of the region and ENSO which is hard to segregate from the impacts of IOD.

Keywords SST · Air-temperature · Thermal coupling · Indian ocean

1 Introduction

The ocean surface acts as a permeable interface for exchanges of heat, water, momentum, gases and other materials in the ocean-atmosphere coupled system. Turbulent exchanges across the air–sea interface play a dominant role compared to molecular diffusion of heat transfer (Sura and Newman 2008). Turbulent heat fluxes are commonly derived with the help of bulk formulae, in which the air–sea thermal gradient is a significant factor. For example, in the case of sensible heat flux, the exchange of heat is proportional to the air–sea temperature difference (Fairall et al. 1996, 2003). Similarly, in computing latent heat flux, air–sea thermal differences indirectly controls the heat exchange through its influence on specific humidity. Besides, air–sea thermal gradient controls the lower atmospheric stability which is another factor controlling the turbulent exchanges between ocean and atmosphere (Fairall et al. (1996, 2003) and references therein). Thus, sea surface temperature (SST) and air temperature (T_{air}) are two fundamental parameters that measure the strength and sign of energy and mass transfer between the two closely coupled components of the climate system at different temporal and spatial scales. The above aspects make air–sea temperature difference, denoted as $T_{diff} = (T_{air} - \text{SST})$, an important parameter in climate studies and projections. Apart from this, T_{diff} is also an important parameter in numerical ocean modelling that uses bulk parametrization to correct wind stress, sensible and latent heat fluxes (Kara et al. 2007).

In the original publication of this article the Fig. 9 was published incorrectly; this error has now been corrected.

✉ Sudheer Joseph
sjo@incois.gov.in

¹ Indian National Centre for Ocean Information Services, Ocean Valley, Pragathi Nagar, Hyderabad 500090, India

² Department of Atmospheric and Oceanic Sciences, University of Colorado, Boulder, CO, USA

At global scale, except for polar and high latitude regions, T_{diff} is negative, indicating that the ocean is emitting heat to the atmosphere (Cayan 1980). However, considerable variability exists in the magnitude and sign of the heat flux on different spatial and temporal scales (Cayan 1980). There have been several past attempts to elucidate the relation between these two variables at different spatiotemporal scales (Roll 1965; Cayan 1980; Basher and Thompson 1996; Kara et al. 2007). Cayan (1980) carried out a detailed analysis of the empirical relation between SST and T_{air} in the North Pacific and North Atlantic from monthly to interannual time scales and found similar patterns of SST and T_{air} variances. He also noted similarities in spatiotemporal patterns of their co-variability in both North Pacific and North Atlantic regions. Kara et al. (2007) carried out a multivariate analysis for finding factors affecting T_{diff} at the global scale using two flux products. A major result of their analysis is that neither SST nor T_{air} exhibits any skill in regulating T_{diff} , and at seasonal time scales T_{diff} is mostly controlled by net solar radiation at the sea surface. This is an important aspect since it is T_{diff} rather than SST or T_{air} , that affect the sign and magnitude of the air–sea turbulent exchanges and thereby air–sea coupling.

To the best of our knowledge, there have been no detailed studies so far analyzing the co-variability of T_{air} and SST in the Indian ocean. The Indian ocean is unique in many oceanographic features mainly due to the seasonal reversal of currents under the influence of the Indian Monsoon system (Schott and McCreary 2001). Studies carried out by Saji et al. (1999) and Webster et al. (1999) hypothesized that large-scale coupled ocean-atmosphere interactions cause inter-annual climate variability in the tropical Indian ocean which has significant ENSO independent component. The above mode of variability was named as the Indian ocean dipole (IOD) which is characterized by an east–west equatorial SST gradient with negative SST anomalies occurring in the southeast tropical Indian ocean off Sumatra-Java coast and positive SST anomalies in the western Indian ocean during its positive phase. Anomalous surface easterly winds accompany these SST anomalies along the equator, together with reduced rainfall in the eastern tropical basin and increased rainfall over the western tropical basin. The IOD is associated with wind-driven upwelling, variation of surface heat fluxes, and reduced eastward transport of mass and heat by the equatorial current (Saji et al. 1999). Equatorial oceanic Rossby and Kelvin waves play important roles in the intensification, duration, and termination of the IOD (Webster et al. 1999).

On intraseasonal time scales, the Madden-Julian Oscillation (MJO); (e.g., Madden and Julian 1994; Hendon and Salby 1994), convectively coupled westward propagating Rossby waves and eastward propagating Kelvin waves

dominate atmospheric intraseasonal oscillations (ISO) (e.g., Wheeler and Kiladis 1999; Chatterjee and Goswami 2004). Krishnamurti et al. (1988) analyzed MONEX data and showed that heat fluxes induced by T_{air} and specific humidity have negligible effects on SST compared to the MJO forced winds. However, later studies using satellite observed outgoing longwave radiation (OLR) showed evidence for the influence of anomalous latent heat fluxes and surface insolation on intraseasonal SST (e.g., Shinoda and Hendon 1998). More recent studies showed that multiple factors like heat fluxes associated with the MJO, oceanic upwelling and advection, and variability of mixed layer also contribute to the intraseasonal SST variability (e.g., Waliser et al. 2003, 2004; Han et al. 2007; Duncan and Han 2009; Vialard et al. 2012).

The importance of turbulent heat fluxes on SST variability and air–sea coupling at various time scales discussed above demonstrates that a careful study of the SST– T_{air} co-variability on multiple timescales over the Indian ocean is needed to understand the detailed picture of ocean-atmosphere coupling and its related processes. In this paper, we focus mainly on sub-monthly to interannual scales of T_{air} –SST relationship over the Indian ocean, particularly on the low correlation between the two variables in the eastern equatorial Indian Ocean (EEIO).

2 Data and methods

In this study, we use SST and T_{air} obtained from TROPFLUX analysis, model simulations and observations. Wind stress data from TROPFLUX is also used in this study. TROPFLUX is derived primarily from the combination of ERA-I (ECMWF interim reanalysis; Dee et al. 2011) data for turbulent and long-wave fluxes, and International Satellite Cloud Climatology Project (ISCCP) (Zhang et al. 2006, 2007) surface radiation data for short wave flux (Kumar et al. 2012). All input products are bias and amplitude-corrected using Global Tropical Moored Buoy Array data, before computation of net surface heat flux and wind stress using the COARE v3 bulk algorithm.

A precise description of the flux computation procedure, as well as a detailed comparison with other daily air–sea heat flux products (OAFLUX, NCEP, NCEP2, ERA-I), is provided in Kumar et al. (2012, 2013). We have chosen the period from 2002 to 2014 as our study window as the source of the SST analysis used in TROPFLUX is improved with data assimilation during this time. However, for interannual study, we make use of monthly means of total data available from 1979 to 2014.

We obtained SST from HYCOM model setup at quarter degree resolution for the Indian ocean (details are available in Joseph et al. 2012). T_{air} is obtained from Navy's

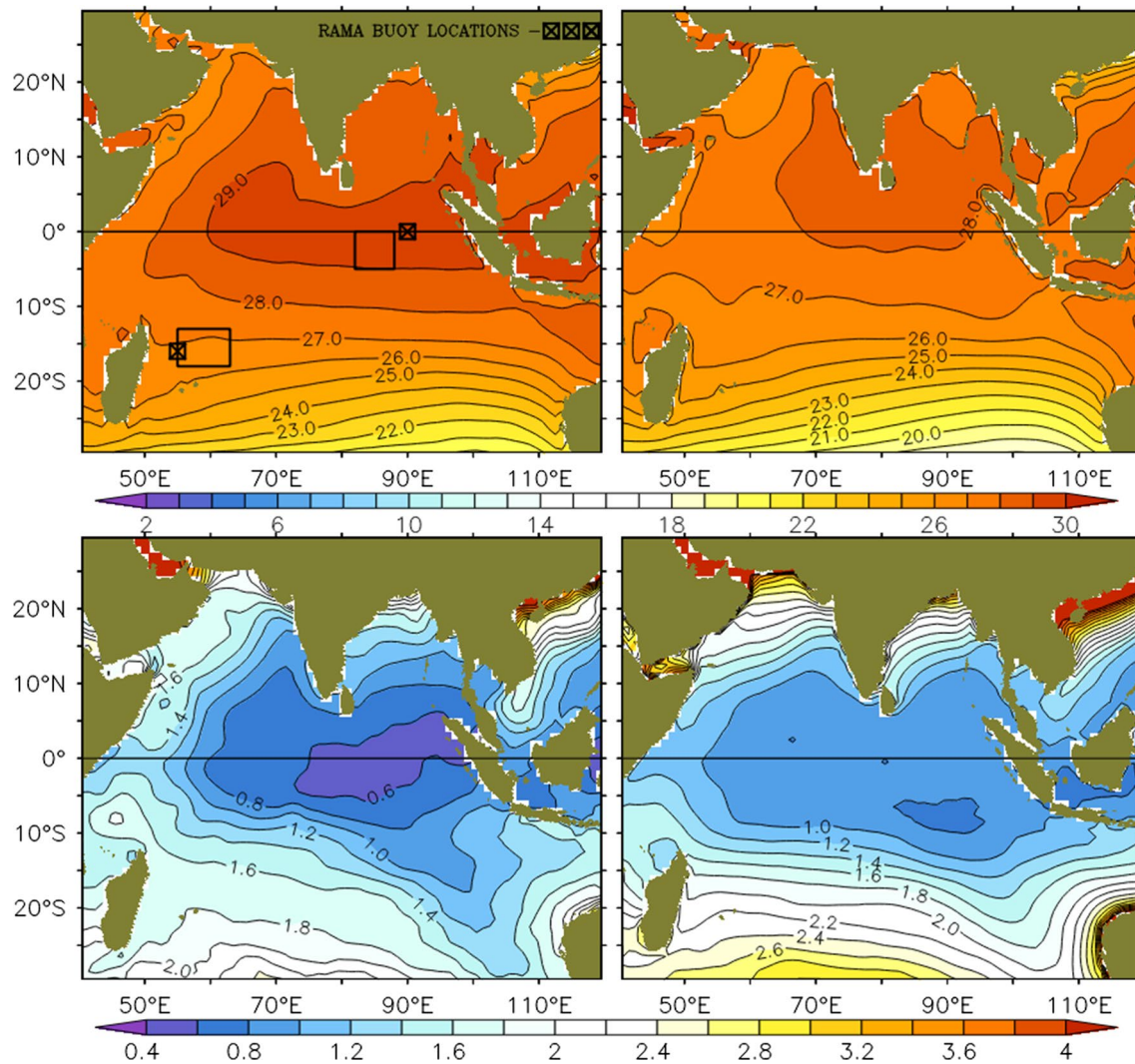


Fig. 1 The mean (*top panels*) and standard deviation (*bottom panels*) of SST (*left*) and Tair (*right*) computed using 11 years of TROPFLUX data from 2002 to 2012. *Color scales indicate SST and Tair*

variability in °C. Location of *box average* used for statistical analysis and near by RAMA buoy locations are marked in *top left panel*

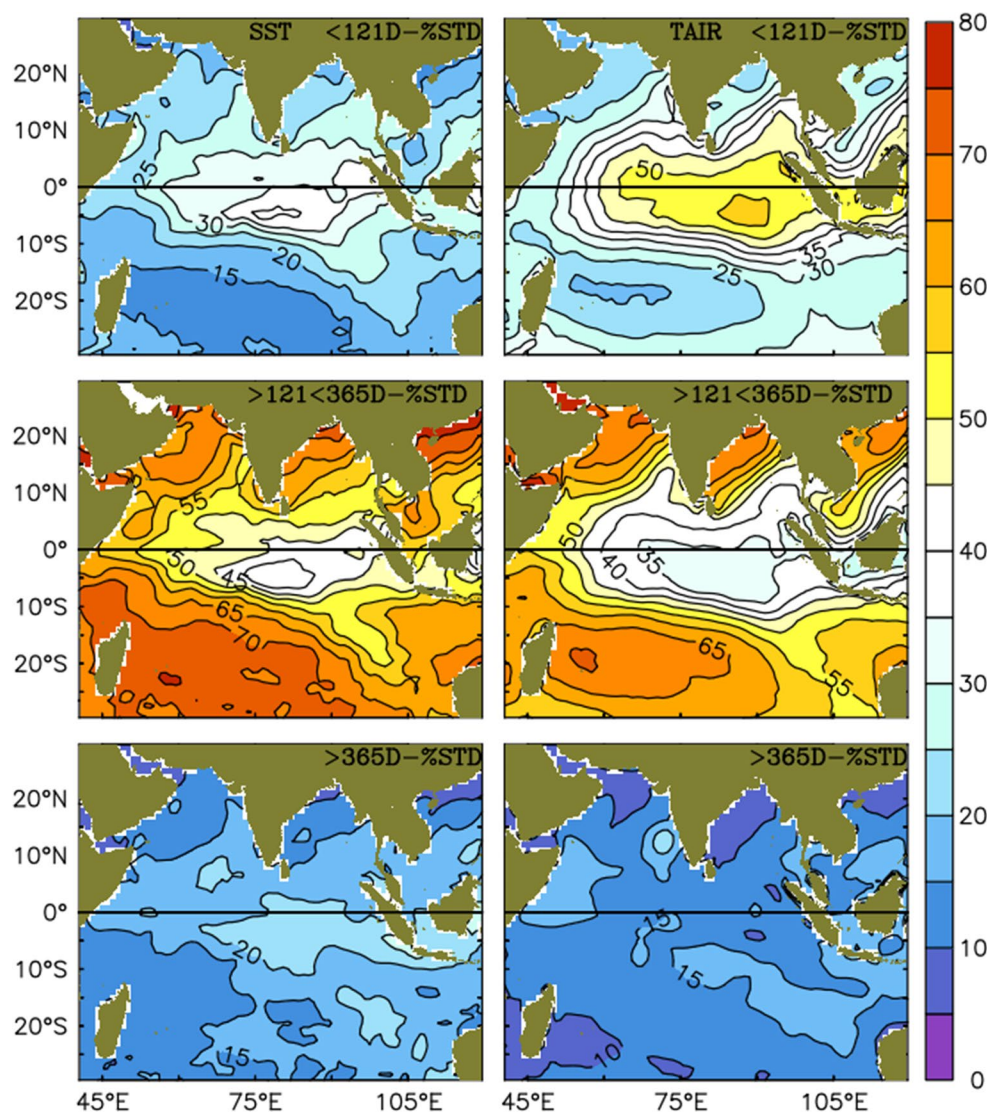
Operational Global Atmospheric Prediction System (NOGAPS) [Numerical Weather Prediction (NWP) model (further referred as HYC-NGP data)]. This secondary source of data was used to verify the correlation results of TROPFLUX data. Wind stress vectors plotted over correlation of HYC-NGP data are from NOGAPS which is used for forcing the model. We have also corroborated the correlation analysis using SST and Tair data from Research Moored Array for African–Asian–Australian Monsoon Analysis and Prediction (RAMA) (McPhaden et al. 2009). Precipitation data of Global Precipitation Climatology Project (GPCP) is obtained from <http://apdrc.soest.hawaii.edu/datadoc/gpcpdaily.php>. We obtained Dipole mode Index (DMI) data from <http://www.jamstec.go.jp/frcgc/research/d1/iod/HTML/Dipole%20Mode%20Index.htm> and Niño-3.4 index from http://www.esrl.noaa.gov/psd/gcos_wgsp/

[Timeseries/Data/nino34.long.anom.data](http://timeseries/Data/nino34.long.anom.data). We have used classification of ENSO and IOD years available at <http://ggweather.com/enso/oni.htm> for the present work.

3 Variability of SST and Tair in the Indian ocean

The basin mean state of SST and Tair distribution in the Indian ocean and their respective standard deviations (STD) using 11 years (2002–2012) of data are presented in Fig. 1. Evidently SST increases from the south and northwest towards the region of maximum in the warm pool of the EEIO (top-left panel of Fig. 1). The climatological maximum of Tair is about 1 °C less than that of SST over the basin (top-right panel). The location of the Tair maximum is notably different from that of SST. While, the SST maximum

Fig. 2 Percentage ratio of standard deviation of SST (*left*) and Tair (*right*) in the intra-seasonal band (<121 days high pass, *row-1*), seasonal band (>121d < 365d, *row-2*) and interannual band (>365 days, *row-3*). Percentage of each band is obtained by dividing respective STDs with total STD multiplied by 100



is approximately symmetric about the equator, the Tair maximum region appears asymmetric with most area locating north of the equator and surrounding India. Thus, the climatological means of SST and Tair have notable differences in their spatial distributions in the Indian ocean.

In contrast to the mean SST that attains its maximum in EEIO, the standard deviation (STD) of SST obtains its minimum in this region. The magnitude of SST-STD increases poleward on both sides of the equator and westward along the equator, a spatial pattern that is roughly opposing to that of the mean SST (compare top-left and bottom-left panels of Fig. 1). Large-scale variability of SST is observed in the southern basin with largest STD value being ≈ 2 °C near 30°S. Near the coasts of East Africa and Oman as well as in the northern Bay of Bengal, SST-STD values exceed 1 °C. The STD pattern of Tair roughly follows the same of the SST (bottom panels of Fig. 1). In general, the STD of Tair is higher than that of SST.

Variability of SST in the Indian ocean consists of intra-seasonal, seasonal and interannual time scales. To understand the patterns of SST and Tair variability on each of these time scales, we have filtered the daily data of SST and Tair using a 121-day high pass filter (ISO), 121 and 365-day band pass filter (seasonal), and 365-day low pass filter (inter-annual), respectively. Using the filtered data, the STD is computed for all three bands. The STD of filtered data at each grid point is divided by the total STD of the 3 bands, which represents the percentage ratio of STD for each band to the total STD (Fig. 2). Interestingly, the patterns of SST and Tair variability, especially their maxima and minima, show marked differences. On intra-seasonal time scales, both Tair and SST variations explain the most of the total variance in the central EEIO, and the percentages decrease away from the EEIO both zonally and meridionally (top panels of Fig. 2). While the ISO band accounts for 30–40 % of the total STD in SST (top-left)

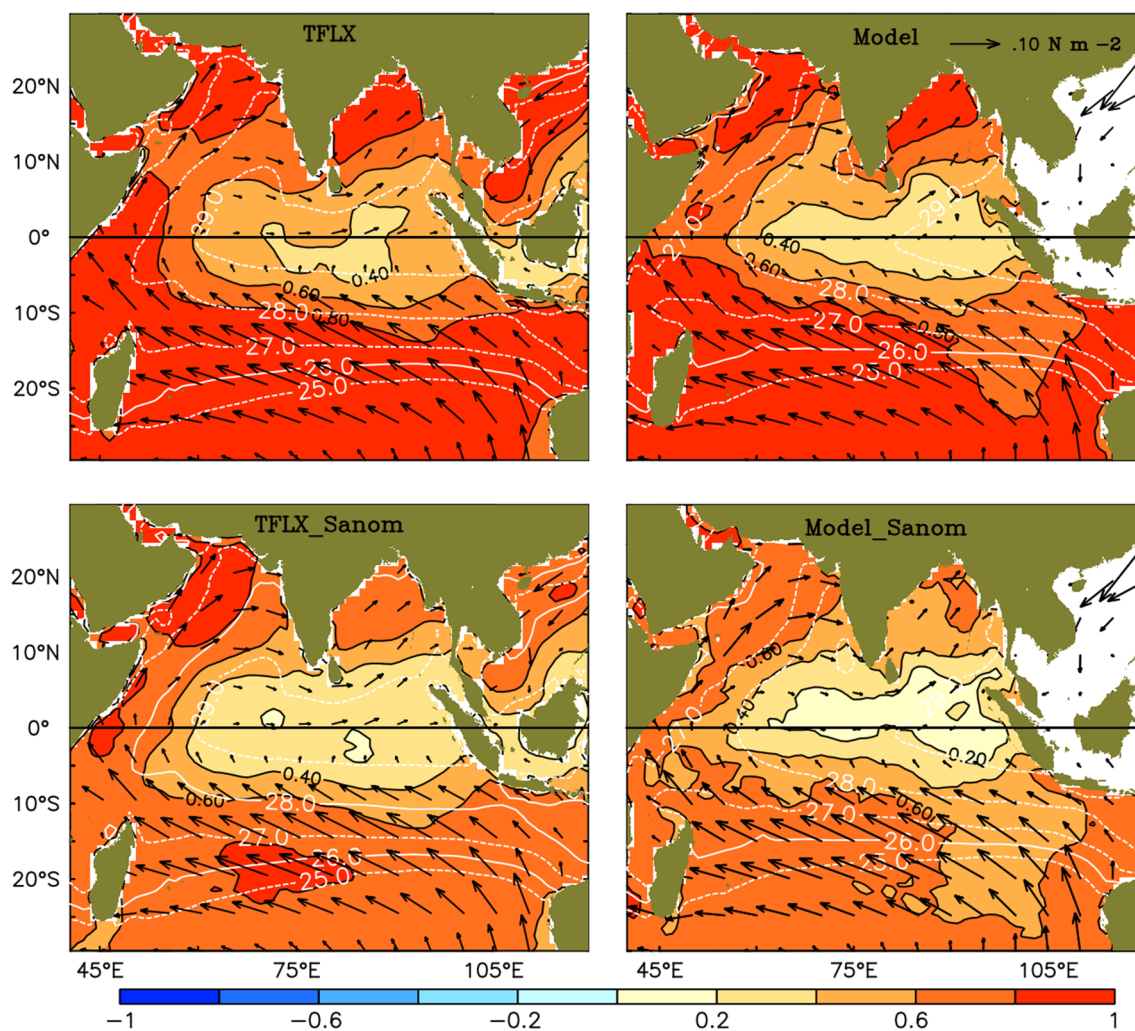


Fig. 3 Correlation of SST and Tair computed using daily TROP-FLUX (left) and model (right) data with seasonal cycle (row-1) and after removal of seasonal-cycle (row-2). Annual mean wind stress

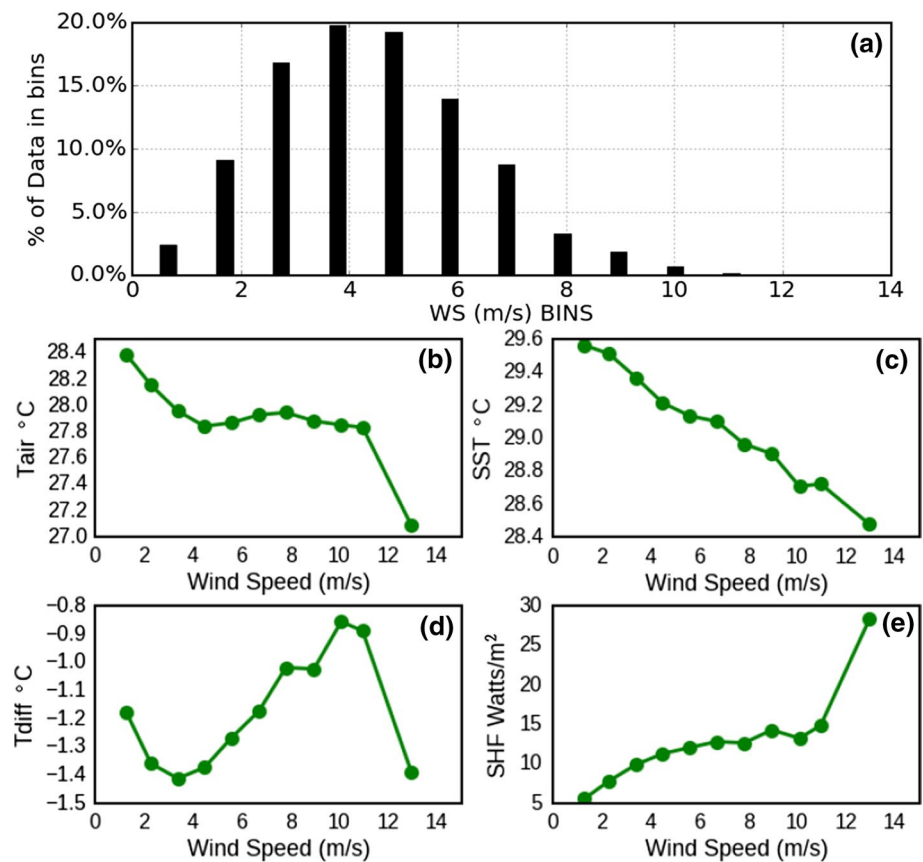
vectors are plotted, and annual mean SST (°C) is contoured over the correlation maps (white dash contours)

in the central-EEIO, Tair explains 45–60 % of total STD in this region, which is approximately 15–20 % more compared to SST. The situation for the seasonal band, however, reverses, with the percentage minima occurring in the central-EEIO for Tair and SST (middle panels of Fig. 2), and SST STD accounting for larger percentages (35–50 %) than Tair STD (30–45 %) relative to their total STDs. On inter-annual time scales, both SST and Tair variations (bottom panels of Fig. 2) obtain the minimum amplitudes comparing to intraseasonal variability and seasonal cycle, explaining 20–25 % total SST STD in the central-eastern equatorial basin south of the equator and 15–20 % Tair STD in the southeast tropical Indian ocean. In difference to the intraseasonal and seasonal variability whose maxima/minima regions collocate, the region of maxima/minima for interannual variability of SST and Tair differ.

4 The perpetual SST–Tair relation and its seasonality

Using eleven years of SST and Tair daily data from TROP-FLUX, we computed correlation between them for the Indian ocean (Fig. 3, top-left panel). Similar correlation analysis was also performed using HYC-NGP data (Fig. 3, top-right panel). The high correlation between SST and Tair is suggestive of tight thermal coupling between ocean and atmosphere (Cayan 1980). The Indian ocean has strong seasonal cycle due to the influence of Indian Monsoon (Wyrski 1973; Cutler and Swallow 1984; Hastenrath and Greischar 1991; Shetye and Gouveia 1998; Shenoi et al. 1999; Schott and McCreary 2001; Shankar et al. 2002; Nagura and McPhaden 2008; Iskandar et al. 2009). To assess the influence of seasonal cycle, we have removed the

Fig. 4 Variability of mean Tair, SST, Tdiff and shf against 11 equal bins of wind speed from its minimum to maximum



“mean” seasonal cycle from both datasets and re-calculated the correlation using the anomalies (Fig. 3, bottom panels). In both the original daily data that include seasonal cycle and anomaly data that exclude the seasonal cycle, the patterns of correlation remain similar with reduced correlations in the EEIO for the anomalies.

The most prominent feature of the correlation maps made from both TROPFLUX and HYC-NGP data with and without the seasonal cycle is the low correlation tongue observed in the equatorial region extending from the eastern boundary to 60°E. Though the correlation is positive, it is intriguing that the correlation drops below 0.5 within this tongue even with seasonal cycle included, when the rest of the Indian ocean shows strong ocean-atmosphere thermal coupling with Tair and SST correlation of $R > 0.8$ (Fig. 3, row-1). Even though the patterns are similar for both datasets, the correlation for HYC-NGP data has noticeable drops, with $R < 0.4$ (Fig. 3, row-1, right) in the EEIO compared to the TROPFLUX map. The SST remains above 28 °C in both TROPFLUX and HYC-NGP data for the entire tongue region. Wind stress vectors of both TROPFLUX and NOGAPS plotted over correlation maps shows a similar pattern on a basin scale. For both data, wind stress is considerably low in the EEIO, where the low correlation of SST & Tair is observed.

In the bulk flux formulation (Fairall et al. 1996, 2003), sensible heat flux (shf) is directly proportional to both wind speed and Tdiff. In cases where Tdiff (absolute value) is < 1 , it reduces the contribution of wind to the shf as Tdiff is a multiplication factor. For regions where Tdiff is > 1 , with high wind speeds, both contribute positively to shf. In the EEIO, we have Tdiff > 1 throughout the year and lower wind speeds, which makes it a case worth examining. Figure 4a shows the histogram of wind speed distribution in EEIO, where 90 % of wind speed values fall below 7 ms^{-1} and mean wind speed is $\approx 4.5 \text{ ms}^{-1}$. Tair, SST, Tdiff, and shf from the EEIO, are plotted against 11 equal bins of wind speed between its minimum ($\approx 0.5 \text{ ms}^{-1}$) and maximum ($\approx 13 \text{ ms}^{-1}$) to understand their behavior under different wind regimes (Fig. 4 (bottom panel)). The plot of Tair against wind speed bins (Fig. 4b) shows that from 0.5 to $\approx 4 \text{ ms}^{-1}$, Tair decreases with increase in wind speed. It further shows a slight increase up to 7 ms^{-1} and after that reduces slightly up to 12 ms^{-1} . However, SST shows a more linear relation and continuously decreases with increase in wind speed (Fig. 4c). The relation of Tdiff with wind speed (Fig. 4d) is expected to be resultant of both Tair and SST. This relationship is highly nonlinear, with a maximum Tdiff (absolute value) of $\approx 1.42 \text{ }^\circ\text{C}$ when wind speed is $\approx 3.5 \text{ ms}^{-1}$ ($\text{shf} < 10 \text{ Watts m}^{-2}$) and minimum of

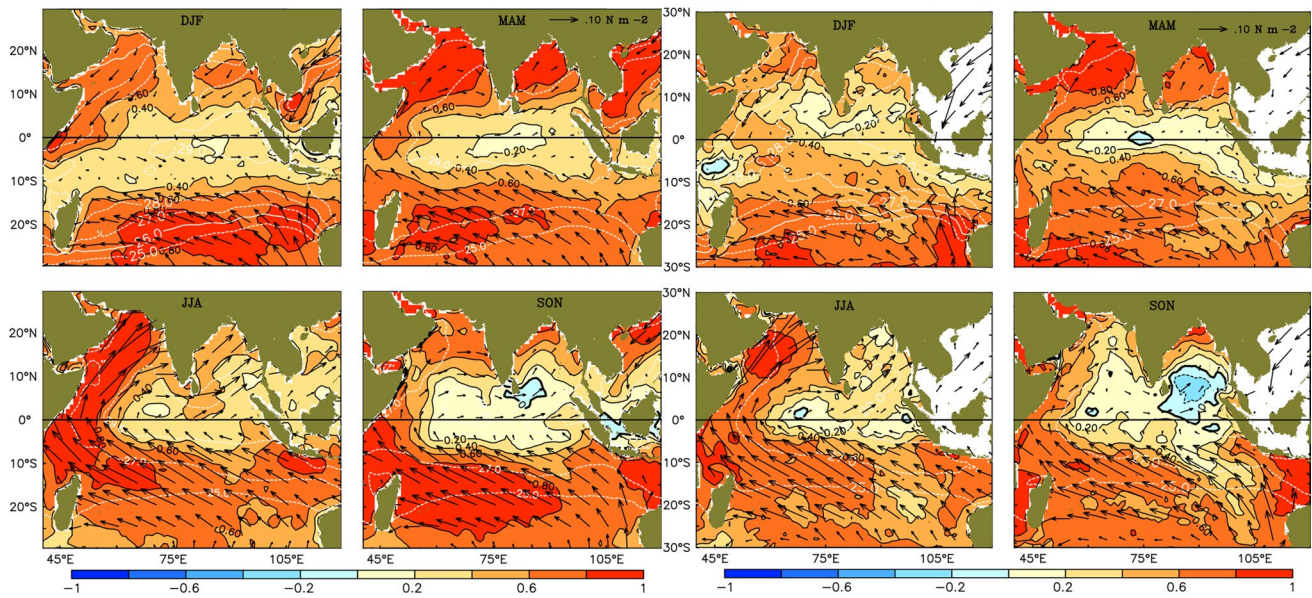


Fig. 5 Seasonal correlation maps of SST and Tair using 11 years of TROPFLUX data (left-4 panels). Same computed using HYCOM SST and Tair from NOGAPS atmospheric forcing used to run the

model (2003–2010) (right-4 panels). Seasonal climatology of wind-stress vectors is overlaid on the correlation map, and mean seasonal SST (°C) is contoured over the maps (white dashed contours)

$\approx 0.85 \text{ }^\circ\text{C}$ when wind speed is $\approx 10 \text{ ms}^{-1}$. Relation of shf with wind speed is reflecting the decrease in SST to a certain extent (Fig. 4e) through its contribution from Tdiff and drag coefficient components in the shf equation. We do not attach much significance to the association of variables to the last bin of wind speed as there is less percentage of data above 12 ms^{-1} . Thus, in the EEIO, both Tair and SST shows almost parallel decreasing tendency for wind speeds up to $\approx 4 \text{ ms}^{-1}$. After that, Tair shows a slight increase up to 7 ms^{-1} as shf increases, while SST continuously reduces with increase in wind speed. However, 90 % of the winds in this area are less than 7 ms^{-1} . The lower wind speed and associated lower shf, therefore compliments the maintenance of larger Tdiff which prevails in this region, though there is non-linear relation exists between wind speed and Tdiff.

In the Indian ocean, there is the directional change of the winds from easterlies in the southern hemisphere to westerlies in the northern hemisphere for seasons other than winter (Schott and McCreary 2001). Associated with the above transition, a region of low annual mean wind-stress is observed east of 60°E along the equator as seen in the maps. Even though the annual mean winds are weak, there is significant interannual variability associated with ENSO/IOD events (Saji et al. 1999), during which there are large amplitude wind stress anomalies in this part of the ocean.

To examine the seasonality of the Tair-SST relationship, we used eleven years SST and Tair daily data from both TROPFLUX and HYC-NGP outputs. We made seasonal bins for December, January, February (DJF); March, April,

May (MAM); June, July, August (JJA) and September, October, November (SON) and computed the correlations for each season (Fig. 5). Lower correlation between SST and Tair in the EEIO is a common feature observed across seasons for both data sets, though the spatial extent of low correlation patch varies among seasons.

During DJF, TROPFLUX data (Fig. 5, left-4 panels) show an area of low correlation extending south-westwards and reaching western boundary of the basin. During this period, winds blow from the northeast, parallel to the African coast, in the Arabian Sea (AS) and Bay of Bengal (BoB). In the south-west Indian ocean, strong south-easterly winds are observed, which meet with the northeasterly winds at about 10°S near the African coast. The confluence of winds from opposite directions results in reduced wind stress from 15°S to 5°S , north of Madagascar and western equatorial Indian ocean (WEIO), forming the inter-tropical convergence zone(ITCZ). SST remains high in the ITCZ region ranging from 28 to $29 \text{ }^\circ\text{C}$. Poor SST -Tair correlation with $R < 0.4$ is observed within ITCZ, over the warm pool. The SST-Tair correlation is much stronger during this time in the south of 15°S , where stronger winds exist, inducing strong mixing and air-sea coupling. The HYC-NGP correlation pattern (Fig. 5, right-4 panels) has differences on the shape of the low correlation region bounded by the $R = 0.4$ contour, though both data sets show generic features of correlation.

During boreal spring (MAM), the direction of winds in the entire northern IO reverses. Winds gain strength in the south-west boundary of the basin, where, winds were

minimum during DJF. The stronger winds impart tight air–sea coupling and the low correlation band ($R < 0.4$) is limited to the east of 50°E . From 70°E to 90°E , the thermal decoupling becomes more prominent with the development of a larger patch of lower correlation ($R < 0.2$). During this season, the contour of the highest SST (29°C) extends to a larger area developing northward, reaching the middle of the eastern AS, hugging the western Indian coastline and crossing to BOB extending up to Myanmar coast. The correlation becomes stronger in the western AS ($R > 0.8$) and in the northern BoB, where there are large areas with ($R > 0.8$). At Southern IO, though the correlation remains higher, the patch of the highest correlation ($R > 0.8$) gets limited between 50°E to 70°E . The gross pattern of spatial correlation in the case of model SST and Tair, in general, shows good agreement with the same of TROPFLUX during MAM.

During the southwest monsoon season (JJA), the Indian ocean is characterized by strong monsoon winds for the entire basin except for the EEIO region. The winds are particularly high on the north-east side of the Madagascar to the south-east coast of Pakistan, inducing strong air–sea thermal coupling as reflected in the strong correlation between the SST and Tair along the western margin of the basin. In general regions of weak winds and high rainfall are associated with low correlation and high winds and low rainfall are associated with higher correlation. However, there are exceptions to this general rule, of between the strong (weak) winds and strong (weak) SST–Tair correlation. For example, towards southeastern side of BoB, the correlation remains weak in spite of winds with moderate speed prevailing there. Thus, during JJA the region of low correlation assumes a crescent shape roughly following rainfall pattern. In the southern Indian ocean, the correlation remains high $R > 0.6$ to large extent, and the $R > 0.8$ contour remains limited to the south-west region of the basin marked by its strong winds and poor rainfall.

During boreal fall (SON), both TROPFLUX and HYC-NGP Tair–SST correlation becomes negative east of Sri Lanka, with HYC-NGP maps showing slightly larger spatial extent compared to the former, which could be due to deficiencies in NWP and HYCOM. However negative correlation observed close to the Sri Lankan coast, in both data sets, could be induced by upwelling and cooling of SST while Tair remains warmer.

The analysis of the seasonal pattern of correlation from both TROPFLUX and HYC-NGP data shows that broadly, the correlation of the former is lower compared to the later. We note that the model setup is at quarter degree resolution and re-gridded to one degree to make it at the same resolution of TROPFLUX, which may have contributed to the differences. However, the larger patterns remains same

across seasons in both data-sets. Thus, the above analysis of correlation maps makes it clear that there is the low correlation between Tair and SST in the EEIO, which is perennial in nature, though there are seasonal changes in pattern and intensity of correlation. Most of the differential variability between SST and Tair causing weak correlation in EEIO exists in the intraseasonal band as evident from $\approx 20\%$ more variability of Tair compared to SST (Fig. 2, row-1). In the seasonal band, Tair shows about 10% less variability compared to the SST.

5 Probability distribution and regression analysis of SST, Tair and Tdiff

Analysis of the Tdiff carried out by Kara et al. (2007) demonstrated that, on a global scale, neither Tair nor SST has control over their differences (Tdiff), but other atmospheric parameters influence the spatiotemporal variability of Tdiff. Given the low correlation observed in the EEIO, we examine the statistical distribution of area average of Tair and SST from EEIO and compare it with that from a high correlation region in the South West Indian ocean (SWIO; refer Fig. 1, top left panel, boxes). Availability of RAMA buoy measurements for SST and Tair from this region also prompted us to choose the area apart from contrasting SST–Tair relation. We also regressed the SST and Tair against Tdiff from EEIO and SWIO to examine the control of each variable on Tdiff.

Figure 6 shows the probability density distribution histograms of SST (green) and Tair (red) from EEIO (left) and SWIO (right). These histograms show probability density of each bin on Y-axis. The probability envelopes plotted over the histograms are generated using the respective means and STD of the individual variables and thus represent the theoretical curve of them if they were following the normal distribution. However, histograms show that there are deviations from the normality particularly in the case of SWIO, where there is a substantial bi-modal distribution of SST and Tair. In the EEIO, Tair distribution is more platykurtic compared to SST. The means of SST are more than 1°C higher, which makes their distributions stand apart. In contrast, the histograms in the SWIO show more comparable distributions with means of Tair and SST just 0.5°C apart.

In the EEIO, STD of both Tair (STD = 0.69) and SST (STD = 0.52) are substantially smaller than those of the SWIO, and among them, SST varies less than Tair. In the SWIO, STD is much higher for both SST (1.6) and Tair (1.69), and hence, normal curves are broader with a platykurtic shape for both variables. The distributions of SST and Tair mostly overlap in the SWIO, which is different from the EEIO where the overlap is much smaller.

Fig. 6 Probability density distributions (histograms) of Tair (red) and SST (green) from EEIO (left) and SWIO (right). Dashed lines shows the theoretical Gaussian curve generated using mean (μ) and standard deviation (σ) of box averages of Tair and SST. Units of SST and Tair are in $^{\circ}\text{C}$

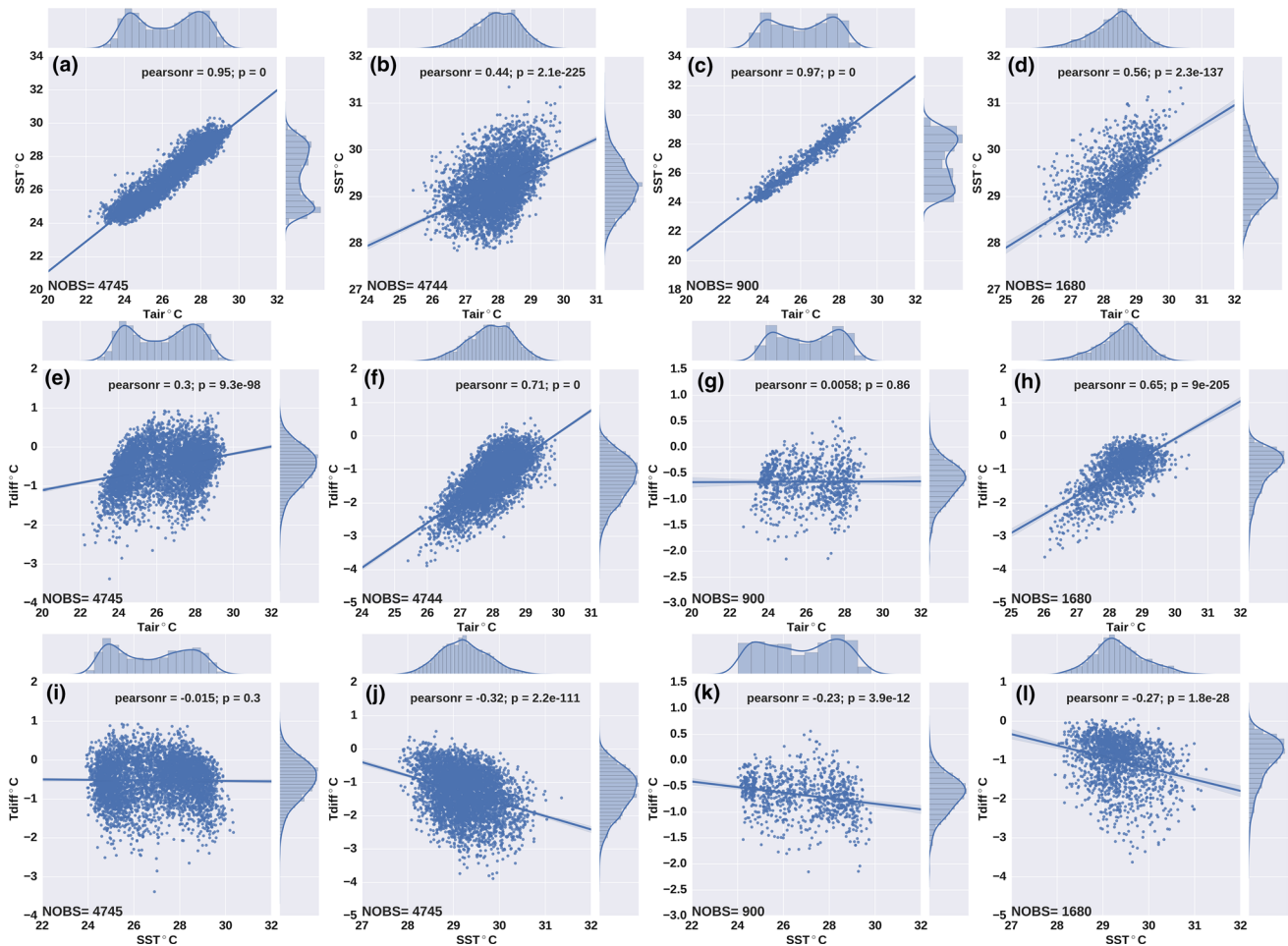
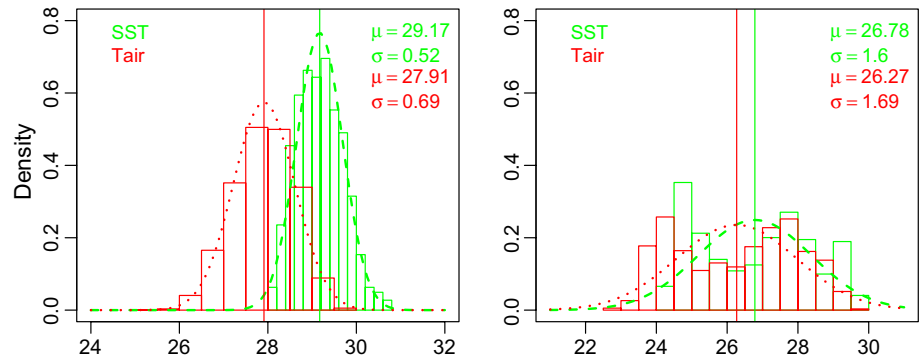


Fig. 7 TROPFLUX [Column-1 & 2] **a(b)**-SST vs. Tair regression from SWIO (EEIO); **c(d)**-RAMA [Column-3&4] SST-vs.-Tair regression from SWIO(EEIO); **e(f)**-Tair-vs.-Tdiff from SWIO(EEIO); **g(h)**-

Tair-vs.-Tdiff SWIO(EEIO); **i(j)**-SST-vs.-Tdiff SWIO(EEIO) and **k(l)**-SST-vs.-Tdiff SWIO(EEIO). *P* value in each plot indicate probability of zero correlation

The scatter plots of Tair vs. SST from SWIO & EEIO with correlation values of 0.9 and 0.44 respectively using TROPFLUX and 0.97 & 0.56, using RAMA buoy data are presented in Fig. 7 (a to d). While the Tair-SST relation in SWIO is comparable to that of global ocean (Kara et al. 2007), EEIO shows evident differences. Tair and SST show

a good linear relationship in the SWIO (Fig. 7 (a and c)), but their relation is nonlinear in the EEIO, with the linear regression lines being significantly different as seen in the scatter diagram. Interestingly, neither Tair nor SST determines Tdiff in the SWIO (Fig. 7 e, g, i, k) with a maximum linear correlation of only 0.3 which is in line with global

scenario. Over the EEIO, however, Tair and Tdiff relationship is more linear than SST-Tair relation (compare Fig. 7, h with b and d) with $R = 0.71$, indicating that Tair is more important in determining Tdiff in this region. However, SST does not have much influence in determining Tdiff as shown by its lower negative correlation of 0.3 and 0.2 (Fig. 7j, l) in TROPFLUX and Rama data respectively.

Thus, over the EEIO, the relation between the Tair and SST is not consistent with the global pattern presented by Kara et al. (2007). In the EEIO almost 100 % of SST data points are higher than Tair with just 32 occurrences of Tair above SST out of 4747 data pairs. The mean of SST is found to be 29.13, and same of Tair is observed to be 27.91, with an average difference of -1.22 °C. Maximum Tdiff found in this area is -3.8 °C.

6 Intraseasonal SST and Tair relation and role of precipitation

The interaction between the upper-ocean and large-scale organised convection plays a dominant role in modulating tropical ISO (Lau and Waliser 2012). Recent studies have shown that, apart from the contribution of variability on intraseasonal timescale, ISOs impact Indian ocean Dipole (IOD), which is an inter-annual mode of variability in the Indian ocean (Saji et al. 1999). Surface westerly anomalies associated with ISOs force downwelling oceanic Kelvin waves, which damp the negative SST anomalies of IOD (Rao 2004; Han et al. 2006). There have been extensive studies on the intraseasonal variability of both ocean and atmosphere from the Indian ocean region. Nevertheless, accurate simulation of atmospheric ISOs and related coupled process are yet to reach a matured state for this tropical ocean basin (Slingo et al. 1996; Lin et al. 2006; Han et al. 2007). With this background and also with an observation of higher percentage ratio of intraseasonal variance at EEIO in both SST and Tair as reported earlier, we have divided the intraseasonal period to sub-monthly and MJO bands to analyse Tair-SST co-variability in these windows.

The EEIO is one of the regions with high rainfall in IO (Fujita et al. 2013). There are several previous studies exploring the relationship between P and SST at different timescales (Meehl 1997; Trenberth and Shea 2005; Wu and Kirtman 2005; Wu et al. 2006; Wu and Kirtman 2007; Roxy and Tanimoto 2012; Roxy et al. 2013). The P-SST relationship depends on the choice of timescale, because of processes linking both variables differ. At biennial scale, enhanced convection feedback to the ocean through winds resulting increased latent heat flux and mixing (Meehl 1997). In the above study, the author showed a resultant reversal of SST anomalies persisted in the oceanic memory

leading to a reversal of rainfall anomalies during the subsequent year. Wu and Kirtman (2007) showed that anomalous convection resulting from higher evaporation and moisture convergence triggered by SST anomalies results in positive SST-rainfall correlation. The authors also argue that anomalous convection can negatively feedback on SST due to increased cloudiness, wind-evaporation, mixing and upwelling, resulting negative rainfall-SST and rainfall-SST tendency correlation. Thus, Wu and Kirtman (2007) suggests seasonal changes in rainfall-SST relation in the Indo-Pacific basins.

The studies by Meehl (1997) and Wu and Kirtman (2007) were using monthly means of both variables and described the evolution of rainfall-SST monthly lead-lag relation through the atmospheric feedback loop. This “longer temporal window” of rainfall and SST relation is distinct from the short term (few days scale) impact of rainfall on SST. At intraseasonal scale, we are focusing on rainfall-SST and rainfall-Tair relation within a lead-lag window of less than 40 days. Previous studies by Han et al. (2007), Duncan and Han (2009), Vialard et al. (2012) explains factors affecting intraseasonal SST variability at the EEIO for different seasons. These studies showed that SST variability in this region is primarily affected by intraseasonal wind speed (through latent and sensible heat fluxes & entrainment) and wind stress (through upwelling and advection). So on a seasonal scale, the above processes rather than P controls the SST variability.

Intraseasonal SST variability associated with mixed layer processes from Indian ocean is examined in several recent studies (Waliser et al. 2003, 2004; Duvel et al. 2004; Duvel and Vialard 2007; Jayakumar et al. 2011; Vialard et al. 2012). Previous efforts to understand the intra-seasonal variability of SST dominated by MJO from the EEIO showed linkages to atmospheric fluxes, horizontal advection, mixed layer depth (MLD) and Barrier layer thickness (BLT) (Schiller and Godfrey 2003; Drushka et al. 2012, 2014). An active phase of MJO shows anomalously deep convection with wavelengths of 12000 – 20000 km coupled to zonal surface winds (Wheeler and Hendon 2004) propagating eastward at a speed of 5 ms^{-1} (Zhang et al. 1995). Zonally, on either side of an active MJO, weak anomalies of convection and wind exists and such phases are described as suppressed MJOs (Drushka et al. 2012). The authors showed that during November to April, MLD variations in MJO timescale modulate approximately 40% of Mixed layer temperature (MLD_T) variability. MLD_T is significantly correlated to net heat flux during active phase with a caveat that MLD_T has only 50-80 % less variance in comparison to the same of net flux (Drushka et al. 2012). The above study also finds that vertical entrainment accounts for almost 50 % of MLD_T variance during active phase of MJO and do not contribute much during suppressed phase.

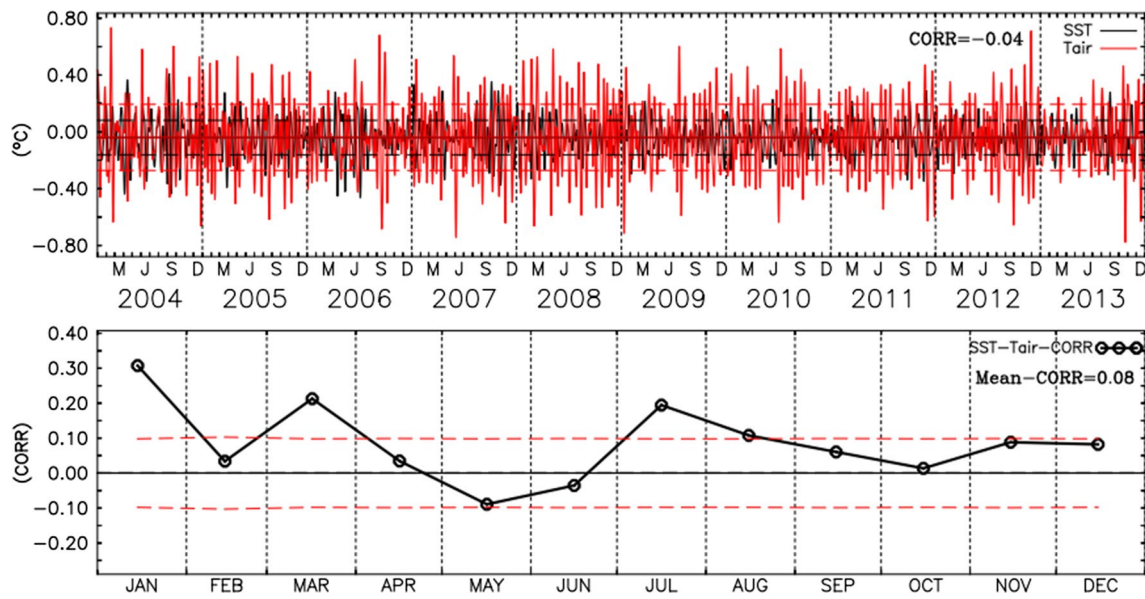


Fig. 8 10–30 day band passed SST and Tair time series (70°E–90°E;3°S–3°N) averaged data (top panel) with respective one standard deviations (dashed lines). Lower panel shows correla-

tions computed for each month using filtered daily data (2003–2013). Dashed red line indicate 95 % significance level of correlation

Heat flux associated with horizontal and vertical convection is found to co-vary with tendency of MLD_T. However, their contribution to the tendency of MLD_T at average MJO time scale is found to be negligible compared to net flux and vertical entrainment (Drushka et al. 2012).

Fresh water input from strong mean P and rivers maintain a perennial thick barrier layer (>25 m) at EEIO, which forms due to differences in haline and thermal stratification in the upper layers of the ocean (Masson et al. 2002). Recent observational study by Drushka et al. (2014) shows BLT variability at sub-seasonal scale exceeds 20 m in the EEIO. Estimate from this study show that MJO forced SST anomalies can be as high as 0.4 °C when barrier layer is thin and it reduces to 0.2 °C, when barrier layer is thick. The authors suggest BLT variability is due to both MLD and isothermal layer depth (ILD) variations in EEIO, where intraseasonal variability is associated with MJO (dominantly), monsoon active break cycles and biweekly oscillations.

Thus, the discussion above shows that the intraseasonal variability of SST in the EEIO is driven by several sub-surface and atmospheric process. In the present study, we focus on the resultant or net SST changes at a given time window and assess its relation with Tair which is measured from the atmosphere where lower thermal inertia prevails.

10–30 days sub-monthly correlation: The relative importance of sub-monthly ISOs and MJOs in driving SST variability in the Indian ocean during boreal winter and summer have been examined by (Han et al. 2006; Duncan and Han 2009; Vialard et al. 2012). Han et al. (2006)

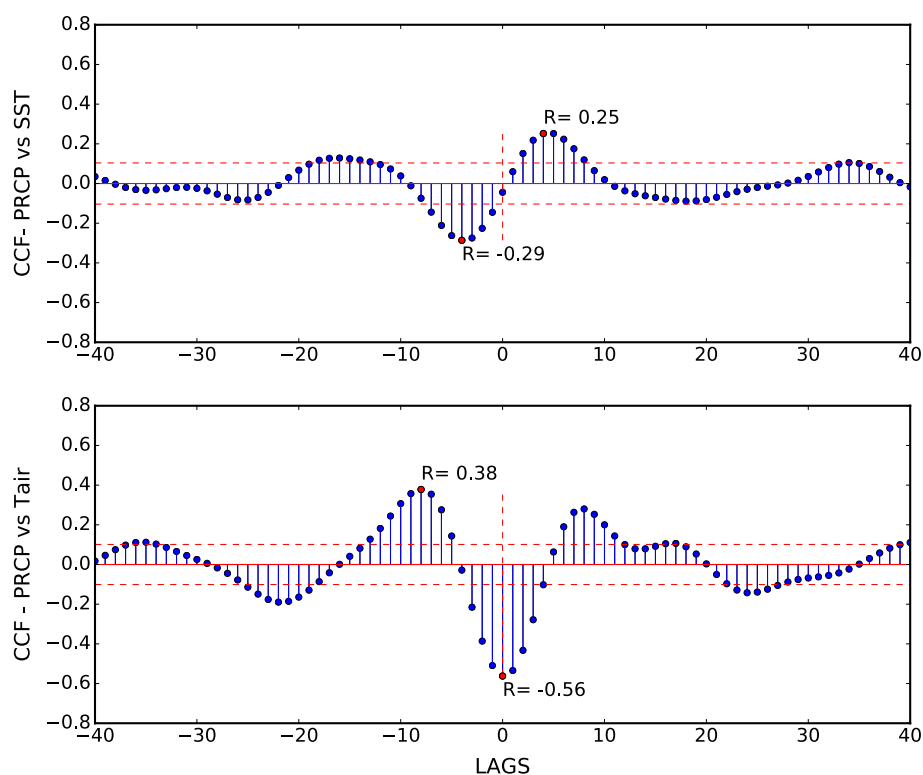
showed that, in spite of stronger winds associated with sub-monthly ISOs compared to the MJOs, more substantial SST variability is associated with the latter. Quasi-biweekly variability forced by sub-monthly ISOs are also reported from the meridional currents of the equatorial Indian ocean (Reppin et al. 1999; Sengupta and Ravichandran 2001; Masumoto 2005; Miyama et al. 2006).

SST and Tair data filtered for 10–30 days period is presented in Fig. 8 (upper panel). Tair shows a larger variability in this band compared to the SST as indicated by its higher STD. There are sub monthly events in Tair data with amplitude as high as 0.7 °C while the same of SST shows maximum value only up to 0.4 °C, indicating rapid and energetic response of Tair to sub-monthly ISOs compared to SST. Such distinct response of these variables result in extremely poor simultaneous correlation between them.

Correlation between Tair and SST is computed for each month taking 11 years of filtered daily data (Fig. 8) (lower panel). The significance level of correlations at 95 % is obtained for each month following Gayen (1951). The correlations are above significant level only for months of January, March and July. Maximum correlation ($R = 0.3$) is for the month of January. Correlation becomes negative for a period from May to mid-June, even though it is not above significant level and values are very low. The mean correlation for all months is just 0.08.

We have used cross correlation function (CCF) analysis for understanding the lead-lag relation of rainfall with SST and Tair. The 95 % significance level of CCF in all cases are obtained following Bretherton et al. (1999). The

Fig. 9 CCF between SST and P (upper panel) and CCF between Tair and P (lower panel), using 10–30 day filtered time series. Red horizontal dashed lines indicate 95 % significance level ($N = 4744$) and vertical dashed line shows R at zero lag. +ve x-axis values shows P lags SST/Tair and -ve values shows P leads SST/Tair



CCF analysis of P vs. Tair and same vs. SST (Fig. 9) shows that Tair has a relatively high simultaneous correlation ($R = -0.56$; Fig. 9, lower panel) with P, indicating a sudden drop in Tair associated with rain, which corroborates previous studies (Bhat 2002; Rahaman and Ravichandran 2013). Tair warms up again after rain and reaches maximum on eighth day as shown by maximum positive correlation ($R = 0.38$). Unlike Tair-P correlation, there is near zero simultaneous correlation between P and SST which is in agreement with previous studies (Han et al. 2007; Duncan and Han 2009). The SST-P CCF (Fig. 9, upper panel) shows that warm SST precedes the rain (indicated by $R = 0.25$ at four-day lead) which is above 95 % significance level. The relation later reverses with maximum negative correlation ($R = 0.29$) on fourth day after rainfall suggesting a drop in SST after rainfall. Signs of our P-SST lead-lag correlations are in agreement with the analysis carried out by Roxy et al. (2013). Previous study by Duncan and Han (2009) showed that, during boreal summer, P has the largest relative amplitude compared to its total variability in the warm pool region (EEIO) for sub-monthly scales. The non-linear relationship between P and SST and relatively linear relation with Tair in the EEIO contributes to SST-Tair minimum correlation. Thus, at sub-monthly scale, P plays a significant role in modulating SST-Tair relation.

30-90 days band passed correlation: Winds associated with MJO induce 30–60 day variability in SST (McPhaden 1982; Kessler 2005). MJOs dominates the 30–90 day

window of atmospheric variability in the Indian ocean (Madden and Julian 1972, 1994; Han et al. 2007). Our analysis of the 30–90 day band-pass filtered data of Tair and SST showed considerable interannual variability in the ISO intensities in 30–90 day period (Fig. 10, upper panel).

ISO events in 30–90 day window are mostly characterized by sharper and higher amplitude variability of Tair compared to SST. However, there are few events, where SST has higher amplitude response compared to Tair. For example, during April–May of 2003 and those months of 2005, SST amplitudes are higher than those of Tair. In the entire period of analysis, both Tair and SST show a maximum number of ISO signals in 2008 crossing the 1-STD limit. As observed from the time series (Fig. 10, upper panel), both Tair and SST have incoherent variability in this window with amplitudes reaching up to $0.5\text{ }^{\circ}\text{C}$. Also, SST has diametrically opposite anomalies compared to Tair during many events. In some cases, multiple light responses in Tair is reflected against a single significant response in SST, in few other cases, SST lags behind Tair and for some events, the lead-lag reverses. Such inconsistent behaviour of Tair and SST contributes to very poor correlation.

The monthly variations in the correlation between filtered Tair and SST is presented in Fig. 10 (lower panel) with significance levels calculated same way as earlier. There is a significant negative correlation in January for this band, unlike the 10–30 day filtered data. Further, a significant negative correlation exists for the month of April and May

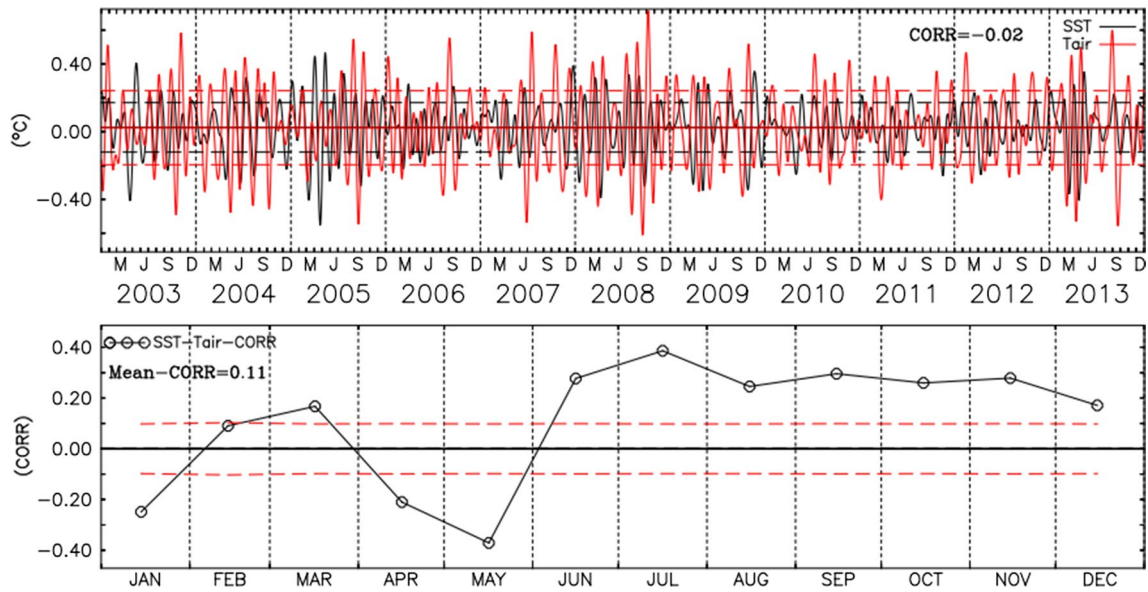
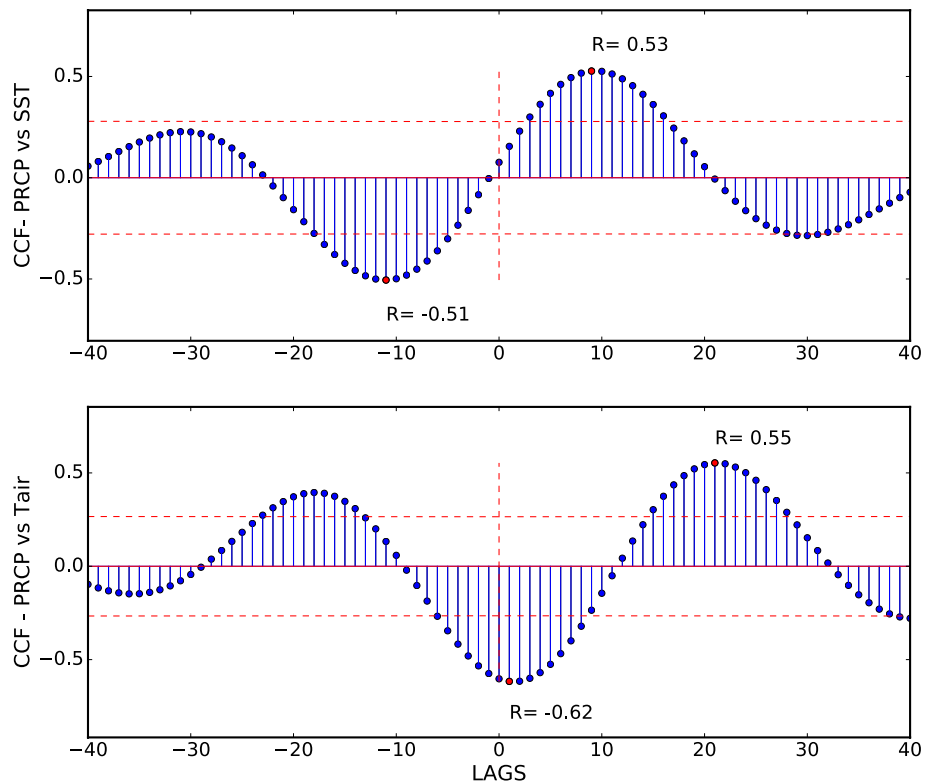


Fig. 10 30–90 day band passed SST and Tair time series (70E–90E:3S–3N) averaged data (*top panel*) with respective one standard deviations (*dashed lines*). *Lower panel* shows correlations computed for each month using filtered daily data (2003–2013). *Dashed red line* indicate 95 % significance level of correlation

Fig. 11 CCF of SST versus P (*upper panel*) and CCF of Tair versus P (*lower panel*), using 30–90 day filtered time series. *Red horizontal dashed lines* indicate 95 % significance level ($N = 4744$) and *vertical dashed line* shows R at zero lag. +ve x-axis values shows P lags SST/Tair and -ve values shows P leads SST/Tair. 100–200 day band passed time series of SST and Tair obtained by averaging selected region with correlation less than 0.45 in the EEIO. *Horizontal dashed lines* indicate respective standard deviations of both SST and Tair



in this band. The maximum positive correlation occurs for the month of July and slightly reduced correlation continues to exist up to December which is weak but significant at 95 % level. The average correlation for the entire period is only 0.11.

We assess the role of P in Tair-SST relationship using the CCF of both variables with rainfall (Fig. 11). For 30–90 day window, SST shows nine days lead ($\max R = 0.53$) to the occurrence of P, indicating the positive contribution of warm SST to subsequent rainfall. SST- P correlation drop to

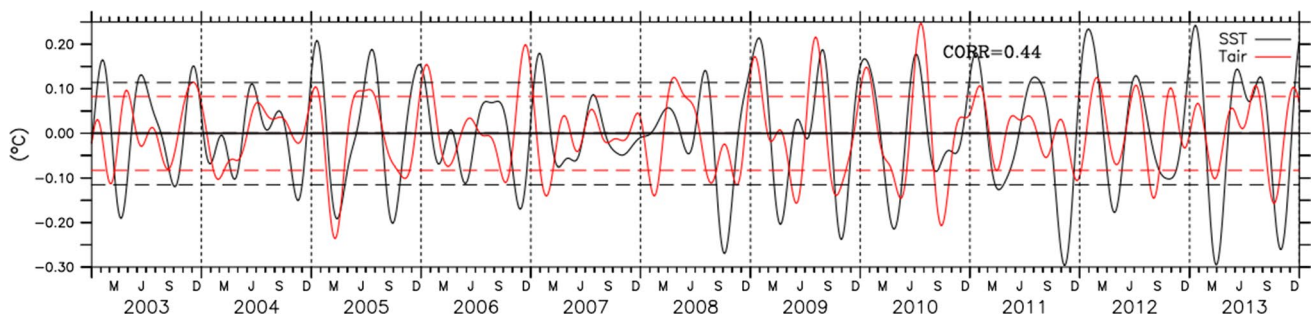


Fig. 12 100–200 day band passed time series of SST and Tair obtained by averaging selected region with correlation less than 0.45 in the EEIO. Horizontal dashed lines indicate respective standard deviations of both SST and Tair

the negative side ($R = -0.51$) 11 days after rain, due to SST cooling after the occurrence of rain. This lagged correlation is close to the 12 days lag reported by Roxy et al. (2013) using 10–90 day filtered data. Interestingly Tair has a different lead-lag relationship with P, and it has relatively stronger ($R = -0.62$) simultaneous negative correlation indicating Tair drop associated with rainfall. However, before 21 days, there is positive correlation suggesting warm Tair leads the rainfall events. Thus, warm SSTA leads to P and after the rain and high winds (i.e. after the passage of MJO), SST cools. These results are consistent with the existing MJO studies (Waliser et al. 1999; Lau and Waliser 2012).

7 Variability of Tair and SST in 100–200 days window

The existence of annual and semi-annual planetary waves in the Indian ocean affects the variability of SST in the EEIO as they induce upwelling/downwelling through their influence on the thermocline (Rao et al. 2010). Propagation of semi-annual Rossby and Kelvin waves and their constructive/destructive interaction (Fu 2007) also affects the variability of SST in the EEIO.

Wyrski jets (Wjs) play a major role in modulating mixed layer thickness and zonal heat transport in the equatorial Indian ocean (Wyrski 1973). The EEIO has a characteristic thinning of the mixed layer associated with equatorial waves and capping of freshwater resulting from heavy P (Han et al. 1999; Gnanaseelan et al. 2012). Previous studies show that barrier layer exists in EEIO as a permanent feature, and it shows variability from intraseasonal to interannual timescales (Sprintall and Tomczak 1992; Masson et al. 2002; Drushka et al. 2014). These studies indicate that barrier layer has a profound influence on SST variability in this region as it can trap heat in the surface layer of the ocean. Cane and Sarachik (1981) and Han et al. (1999) showed that reflected Rossby waves enhance the jets if the wind is periodic and constructively resonate with the wind forcing. The enhancement

happens because, by the time reflected Rossby waves propagate back to the interior ocean, winds change direction during normal wind conditions of the EEIO. The processes described above have a strong influence on the SST in the region.

Tair and SST data were filtered with 100 and 200 days as bounds to examine differences in sub-annual variability of both variables above intraseasonal scale. In this case, time series of SST and Tair are constructed by area averaging of data from EEIO, where correlation is less than 0.45 (Fig. 12). A notable difference in this case compared to other bands examined is the lower STD of Tair compared to SST (Fig. 12). As in the case of intraseasonal bands, there are instances of Tair having opposite anomalies compared to SST, which reduces the correlation between them. A correlation of 0.44 implies that Tair can explain only 19.3 % variability of SST, which is intriguing at this low-frequency band.

Spatially, the lower correlation region of 100–200 day band in the EEIO has a tongue-shaped structure with more or less same spatial extent as in the case of raw data. However, there are three centres of minimum correlation within the larger tongue (Fig. 13 (top left panel)). We have constructed time series by averaging SST and Tair data from three boxes of minimum correlation marked in Fig. 13 (top left panel). Fast Fourier Transforms (FFTs) were computed to analyse dominant modes of variability from them. Further, the percentage of variance attached to each frequency were calculated and plotted against period (Fig. 13; Variances are within 100–200-day band, which excludes annual cycle). Box B:1 shows SST with a strong semi-annual spectral peak of 59 % variance associated with semiannual Wjs and related mixed layer and wave dynamics, corroborating previous study (Han et al. 1999). In the case of Tair, at 121-day frequency, there is a prominent peak, which explains 25 % of the variance. Previous studies showed that winds from the equatorial Indian ocean have significant energy at 120 days frequency (Fu 2007; Girishkumar et al. 2013). However, it is not clear from the present analysis that how it selectively influences Tair at box B:1. Apart from this, Tair also shows another sharp peak with 9 % variance at 106 day period.

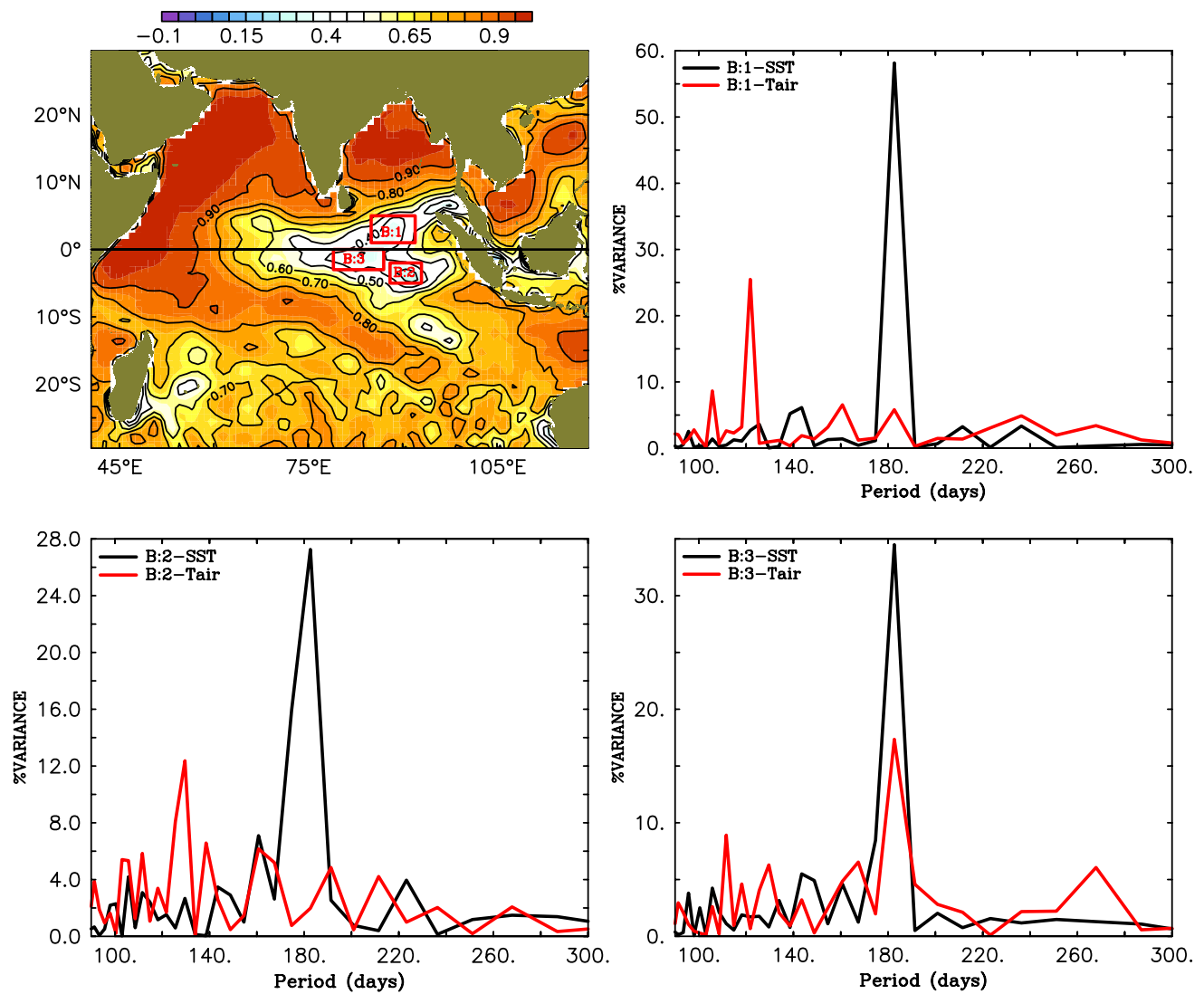


Fig. 13 Correlation map of 100–200 days band pass filtered SST-Tair data (*top-left panel*). B1, B2 and B3 are 3 boxes of minimum correlation centers selected for FFT analysis presented in rest of the panels

The SST from the box: B:2, south of the equator also shows semi-annual frequency as the dominant mode of variability in SST with 28 % of the variance. Tair has no spectral peak at this frequency. Nevertheless, Tair has energy distributed in multiple peaks lower than 140 days contributing to minimum correlation between them.

SST from box B:3 has 40 % variance in the semi-annual frequency, with its location falling on the equator. In contrast to north and south boxes, Tair shows a relatively higher percentage (16 %) of semiannual variance here. Tair also shows spectral peaks with 9 and 6 % variances at 112 and 130 days respectively at this location. Semiannual variations of SST is influenced by zonal current along the equator either directly (advection) or by exciting Rossby waves at the eastern boundary (Godfrey and Panel 1994). Though planetary waves exist in the atmosphere, there is no such

mechanism in the atmosphere which reflects waves on the eastern boundary of IO as in the case of the ocean. CCF analysis of SST and Tair against precipitation in this window did not produce significant correlations. Thus, analysis of SST and Tair in 100–200 days window shows that at the semiannual frequency, Wjs and planetary waves modulate SST which is in agreement with previous studies, whereas, Tair variability in the above frequency is less pronounced.

8 Variability of Tair and SST at interannual timescales

In order to understand the behavior of Tair and SST at various timescales from the EEIO, we have computed cross wavelet coherence (Grinsted et al. 2004) of box averaged

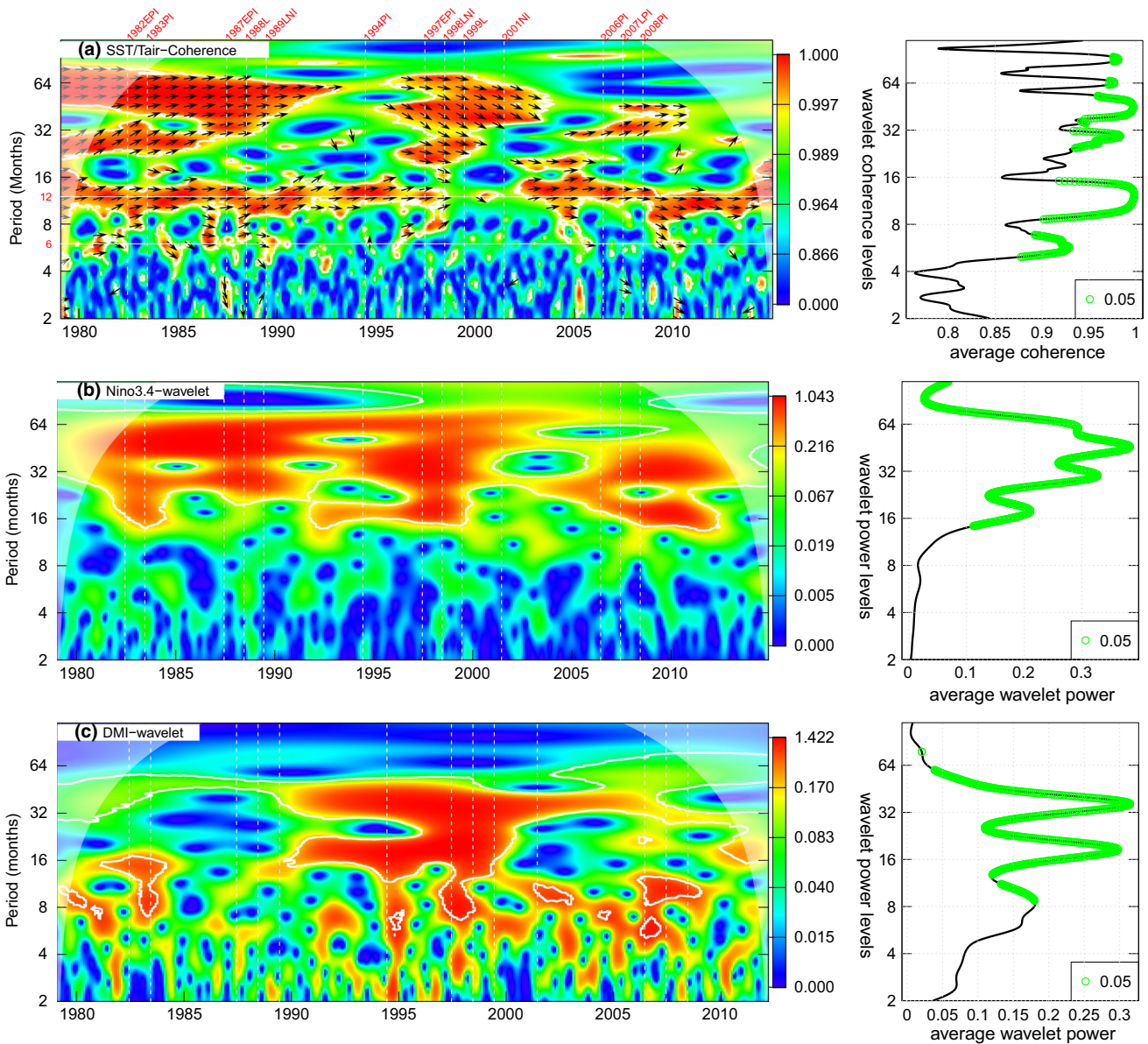


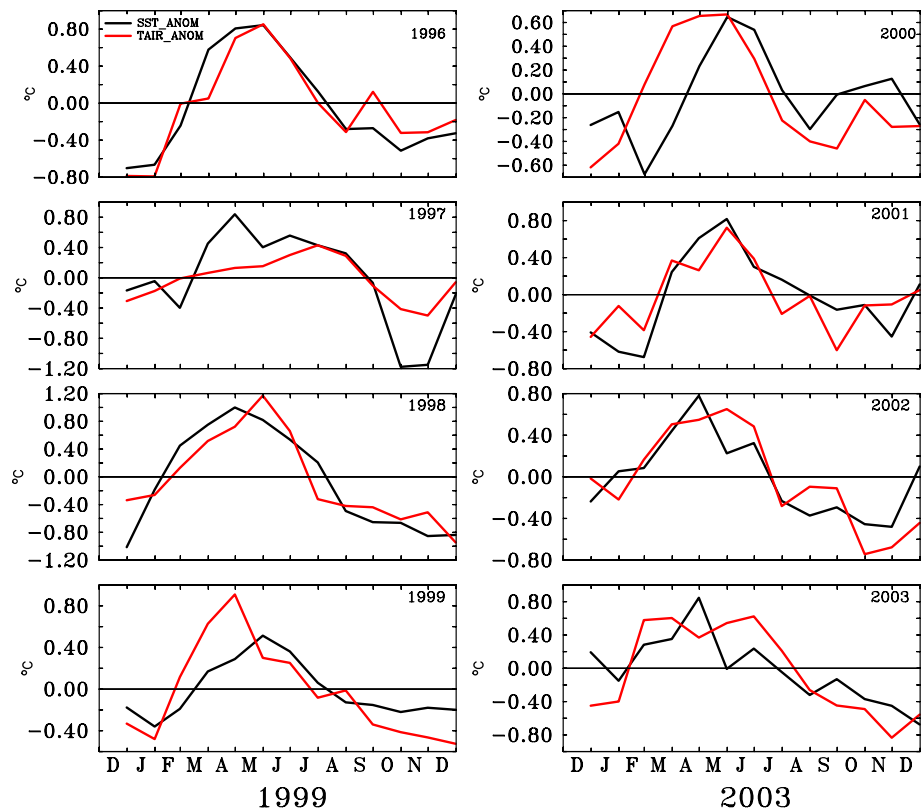
Fig. 14 **a** Wavelet coherence computed using monthly mean time-series of SST and Tair from EEIO. *Arrows* indicate phase angle, which are plotted where they are significant at 95 %. *White color contours* indicate coherence significant at 95 %. *Cone of influence* is indicated by semi-transparent white envelope. *Plots in (black line)* second column shows average coherences corresponding to each frequency in respective locations. *Green circle envelope* indicate aver-

age coherence significant at 95 %. Major interannual events happened during the period of analysis is marked with their year (*white dashed vertical lines*) and *codes in red color* at top horizontal axis (*EPI* = El-Niño + Positive IOD, *PI* = Positive IOD, *L* = La Niña, *LNI* = La Niña + Negative IOD, *NI* = Negative IOD). **b** Wavelet power of Niño-3.4 index and **c** wavelet power of DMI (only up to 2012)

time series of them from the EEIO. We have also computed wavelet power using indices of Niño-3.4 and Dipole mode Index (DMI) (DMI only up to 2012 available at the source; Fig. 14, panel b and c respectively). Figure 14a shows a significant variability of coherence from semi-annual to inter-annual scale. The arrows show relative phases (lead/lag) of SST and Tair. Arrows heading east (west) indicate both SST and Tair are in phase (out of phase). Arrows pointing northeast (southeast) indicate SST (Tair) leads Tair (SST)

and are in phase. Arrows heading northwest (southwest) indicate Tair (SST) leads SST (Tair) and they are out of phase. Following the above convention, the time-varying phases of SST leading Tair (arrows heading slightly northeast and later become perfectly eastward by 2005) at the annual frequency are observed during years 1985, 1990, 2005 and 2010. At annual frequency, coherence is relatively persistent at EEIO, though it becomes discontinuous from 1997 to 2003. From year 2003 onward, the coherence at

Fig. 15 Yearly evolution of monthly Mean SST & Tair anomalies in EEIO



the annual frequency is relatively continuous. Comparison of Fig. 14a, b shows correspondence between enhanced power of Niño3.4 index and the coherent variability of SST and Tair. As the energy of IOD index (Fig. 14c) is observed in similar periods of ENSO, it is difficult to isolate contribution of IOD to SST-Tair coherence. A notable feature of the coherence pattern is the absence of it, at the annual frequency between 1997 to 2003, from the year of the largest IOD of the century occurred together with El-Niño.

There are other lower frequencies where, significant coherence exist between Tair and SST, for example from 1985 to 1990, at biennial (24 months) frequency, both SST and Tair show significant coherence with SST having a slight lead over Tair. There is high coherence around pentadal (60 months) frequency, with associated changes in phase relation between Tair and SST. The broad band of pentadal coherence reduces considerably for a short period between 1992 and 1995 corresponding to the reduced wavelet power of Niño3.4 (Fig. 14a, b). The wavelet power of Niño3.4, and DMI intensify close to 1997 and continues up to 2002, but coherence of Tair-SST occurs with Tair slightly leading SST.

In order to understand gap in annual coherence observed in Fig. 14a starting from 1997, we have plotted monthly timeseries anomalies of Tair and SST from 1996 to 2003 (Fig. 15). For non-IOD years, timing of Tair maximum coincide with SST maximum and occurs during May contributing to annual coherence. For the year 1997, only SST

maximum (0.8 °C) occurred during the month of May and maximum of Tair happened during early August, when SST anomalies also showed comparable values. Thus, instead of the normal period of coherence during May, it is observed during August–October in 1997. For the subsequent year, the lead of SST to Tair got reduced to one month. During 1999 (La Niña year) the lead-lag relation reverses and it is observed that Tair maximum leads SST maximum, which is contrary to other years. Thus, Tair-SST co-variability occurs during years of ENSO & IOD events with a shift in their normal period. The details of their relation need to be explored in depth which is not in the scope of the present study.

The average coherence plotted in the Fig. 14 on the top right-hand side panel shows no significant coherence for periods less than the semi-annual frequency in the EEIO. Further, the coherence (significant at 95 %) observed at annual, and other lower frequencies are with several discontinuities. Thus, in the EEIO, the coherence between Tair and SST occurs dominantly in annual and lower frequencies characterized by substantial variability and changes in phase relation.

9 Summary and conclusions

In this paper, we present evidence for instantaneous ocean-atmosphere thermal decoupling in the EEIO indicated

by lower correlation of Tair and SST in the region using TROPFLUX data. The results are confirmed using HYC-NGP model data and observations from RAMA buoys. The analysis demonstrates that a perpetual low correlation region co-located with lower wind-stress and lower shf exists in the EEIO. The region is also characterized with highest SSTs in the basin. The reasons for the low correlation in the EEIO is investigated at sub-monthly, intraseasonal, seasonal and interannual time scales. Although it is quantitatively small, we also examine the source of minimum correlation observed in the EEIO.

The overall stronger linear relation of Tair with Tdiff indicate the dominant role of Tair over SST in the maintenance of Tdiff in the EEIO, in contrast to the rest of the Indian ocean and to the global Ocean, where neither SST nor Tair has control over Tdiff (Kara et al. 2007).

At sub-monthly scale, the correlation between Tair and SST is very low. Precipitation plays a significant role in the rapid decrease of Tair, with no such drop in SST. Thus, P acts as a catalyst to the lower correlation through its more linear relation with Tair compared to the non-linear SST-rain relationship at sub-monthly scale.

The SST variability associated with MJO wind forcing in the EEIO is half that of other regions with strong wind forcing (Han et al. 2007). They attribute lower control of the wind on SST to the thicker mixed layer during boreal winter at the EEIO, where it needs much more substantial fluxes to impart a unit change in the magnitude of SST. The more humid and near saturated atmosphere over the warmer ocean with higher SST reduces the dependence of SST on winds through fluxes (Han et al. 2007). However, warmer SST leads to P, a rapid drop in Tair and delayed response in SST after the passage of MJO, resulting lower correspondence between them. Thus, the low-intensity ocean-atmosphere exchanges in the EEIO indicated by the low correlation between SST and Tair occurs in a conducive environment described above.

As the winds are minimum in the EEIO, the remote forcing imparted by waves along the equatorial wave-guide play a larger role in determining the thermal structure of the EEIO compared to direct thermal forcing through fluxes or wind mixing. The remote dynamical forcing dominantly operates in the region at semi-annual frequency through equatorial waves. Such indirect forcing through waves contributes to semi-annual spectral peaks observed in the SST from box B1 & B2 in Fig. 13. However, no such semi-annual variability is found in Tair, which has different forcing mechanism compared to SST. Thus, in the EEIO, the wave-induced thermal changes in ocean surface not mimicked by the atmosphere contributes to low correlation at the semi-annual frequency.

The analysis of Tair and SST at higher frequencies revealed that there is a negligible contribution to the

correlation between Tair and SST from those scales. It leaves the question open about the source of limited correlation observed in the EEIO. Wavelet analysis of SST and Tair showed that relatively higher coherence exists between them during ENSO-IOD events, though there is lower co-variability at other frequencies below annual periodicity. Thus, ENSO-IOD events manifest as positive contributors to SST-Tair correlation at inter-annual scale, while breaking it at the annual frequency. The annual warming of the EEIO is the main contributor to the limited correlation observed in the EEIO during non-IOD/ENSO years. The above results warrant an in-depth analysis of co-variability between SST and Tair during events of IOD and ENSO, which will be a future work of utmost interest to the understanding of coupled ocean-atmosphere processes.

Acknowledgments Ministry of Earth Sciences and Director INCOIS are acknowledged for the infrastructural support. Authors wish to acknowledge use of the Ferret program for data analysis and graphics in this paper. Ferret is a product of NOAA's Pacific Marine Environmental Laboratory. (Information is available at <http://ferret.pmel.noaa.gov/Ferret/>). We thank editor Dr. Jean-Claude Duplessy and three anonymous reviewers for their valuable suggestions and comments which improved the quality of this work. Colleagues from MOG group at INCOIS are acknowledged for their support. This is INCOIS Publication NO: 266.

References

- Basher RE, Thompson CS (1996) Relationship of air temperatures in New Zealand to regional anomalies in sea-surface temperature and atmospheric circulation. *Int J Climatol* 16(4):405–425. doi:10.1002/(SICI)1097-0088(199604)16:4<405::AID-JOC14>3.0.CO;2-T
- Bhat GS (2002) Near-surface variations and surface fluxes over the northern bay of bengal during the 1999 Indian summer monsoon. *J Geophys Res: Atmos* 107(D17):ACL 6-€œ1–ACL 6-€œ19. doi: 10.1029/2001JD000382
- Bretherton CS, Widmann M, Dymnikov VP, Wallace JM, Bladé I (1999) The effective number of spatial degrees of freedom of a time-varying field. *J Clim* 12(7):1990–2009. doi:10.1175/1520-0442(1999)012<1990:TENOSD>2.0.CO;2
- Cane MA, Sarachik E (1981) Response of a linear baroclinic equatorial ocean to periodic forcing. *J Mar Res* 39(4):651–693
- Cayan DR (1980) Large-scale relationships between sea surface temperature and surface air temperature. *Mon Weather Rev* 108(1293–1301):1081. doi:10.1175/1520-0493(1980)293:LSRB SS2.0.CO;2
- Chatterjee P, Goswami B (2004) Structure, genesis and scale selection of the tropical quasi-biweekly mode. *Q J R Meteorol Soc* 130(599):1171–1194. doi:10.1256/qj.03.133
- Cutler A, Swallow J (1984) Surface currents of the Indian ocean (to 25°S, 100°E): compiled from historical data archived by the Meteorological Office Bracknell, UK. Technical Report 187, Institute of Ocean Sciences, Institute of Oceanographic Sciences, Wormley, UK
- Dee DP, Uppala SM, Simmons AJ, Berrisford P, Poli P, Kobayashi S, Andrae U, Balmaseda MA, Balsamo G, Bauer P, Bechtold P, Beljaars ACM, van de Berg L, Bidlot J, Bormann N, Delsol C, Dragani R, Fuentes M, Geer AJ, Haimberger L, Healy SB, Hersbach H, Holm EV, Isaksen L, Kallberg P, Kohler M, Matricardi

- M, McNally AP, Monge-Sanz BM, Morcrette JJ, Park BK, Peubey C, de Rosnay P, Tavolato C, Thepaut JN, Vitart F (2011) The era-interim reanalysis: configuration and performance of the data assimilation system. *Q J R Meteorol Soc* 137(656):553–597. doi:10.1002/qj.828
- Drushka K, Sprintall J, Gille ST, Wijffels S (2012) In situ observations of Madden–Julian oscillation mixed layer dynamics in the Indian and Western Pacific Oceans. *J Clim* 25(7):2306–2328. doi:10.1175/jcli-d-11-00203.1
- Drushka K, Sprintall J, Gille ST (2014) Subseasonal variations in salinity and barrier-layer thickness in the eastern equatorial Indian ocean. *J Geophys Res Oceans* 119(2):805–823. doi:10.1002/2013jc009422
- Duncan B, Han W (2009) Indian ocean intraseasonal sea surface temperature variability during boreal summer: Madden–Julian oscillation versus submonthly forcing and processes. *J Geophys Res*. doi:10.1029/2008jc004958
- Duvel JP, Vialard J (2007) Indo-pacific sea surface temperature perturbations associated with intraseasonal oscillations of tropical convection. *J Clim* 20(13):3056–3082. doi:10.1175/jcli4144.1
- Duvel JP, Roca R, Vialard J (2004) Ocean mixed layer temperature variations induced by intraseasonal convective perturbations over the Indian ocean. *J Atmos Sci* 61(9):1004–1023. doi:10.1175/1520-0469(2004)0611004:omltvi2.0.co;2
- Fairall C, Bradley E, Rogers D, Edson J, Youngs G (1996) Bulk parameterization of air-sea fluxes for tropical ocean-global atmosphere coupled-ocean atmosphere response. *Geophys Res* 101:3747–3764. doi:10.1029/95JC03205
- Fairall C, Bradley EF, Hare J, Grachev A, Edson J (2003) Bulk parameterization of air-sea fluxes: updates and verification for the coare algorithm. *J Clim* 16(4):571–591. doi:10.1175/1520-0442(2003)016<0571:BPOASF>2.0.CO;2
- Fu LL (2007) Intraseasonal variability of the equatorial Indian ocean observed from sea surface height, wind, and temperature data. *J Phys oceanogr* 37(2):188–202. doi:10.1175/JPO3006.1
- Fujita M, Takahashi HG, Hara M (2013) Diurnal cycle of precipitation over the eastern Indian ocean off Sumatra Island during different phases of Indian ocean dipole. *Atmos Sci Lett* 14(3):153–159. doi:10.1002/asl2.432
- Gayen AK (1951) The frequency distribution of the product moment correlation coefficient in random samples of any size drawn from non-normal universes. *Biometrika* 38(1–2):219–247. doi:10.1093/biomet/38.1-2.219
- Girishkumar MS, Ravichandran M, Han W (2013) Observed intraseasonal thermocline variability in the Bay of Bengal. *J Geophys Res Oceans* 118(7):3336–3349. doi:10.1002/jgrc.20245
- Gnanaseelan C, Deshpande A, McPhaden MJ (2012) Impact of Indian ocean dipole and el niño/southern oscillation wind-forcing on the warty jets. *J Geophys Res*. doi:10.1029/2012jc007918
- Godfrey JS, Panel OOSD (1994) The role of the Indian ocean in the global climate system: recommendations regarding the Global Ocean Observing System. Ocean Observing System Development Panel, College Station
- Grinsted A, Moore JC, Jevrejeva S (2004) Application of the cross wavelet transform and wavelet coherence to geophysical time series. *Nonlin Process Geophys* 11(5/6):561–566. doi:10.5194/npg-11-561-2004
- Han W, McCreary JP, Anderson DLT, Mariano AJ (1999) Dynamics of the eastern surface jets in the equatorial Indian ocean. *J Phys Oceanogr* 29(9):2191–2209. doi:10.1175/1520-0485(1999)029<2191:DOTESJ>2.0.CO;2
- Han W, Liu WT, Lin J (2006) Impact of atmospheric submonthly oscillations on sea surface temperature of the tropical Indian ocean. *Geophys Res Lett*. doi:10.1029/2005gl025082
- Han W, Yuan D, Liu WT, Halkides DJ (2007) Intraseasonal variability of Indian ocean sea surface temperature during boreal winter: Madden–Julian oscillation versus submonthly forcing and processes. *J Geophys Res*. doi:10.1029/2006jc003791
- Hastenrath S, Greischar L (1991) The monsoonal current regimes of the tropical Indian ocean: observed surface flow fields and their geostrophic and wind-driven components. *J Geophys Res: Oceans* (1978–2012) 96(C7):12,619–12,633. doi:10.1029/91JC00997
- Hendon HH, Salby ML (1994) The life cycle of the Madden–Julian oscillation. *J Atmos Sci* 51(15):2225–2237. doi:10.1175/1520-0469(1994)051<2225:TLCOTM>2.0.CO;2
- Iskandar I, Masumoto Y, Mizuno K (2009) Subsurface equatorial zonal current in the eastern Indian ocean. *J Geophys Res*. doi:10.1029/2008jc005188
- Jayakumar A, Vialard J, Lengaigne M, Gnanaseelan C, McCreary JP, Kumar BP (2011) Processes controlling the surface temperature signature of the Madden–Julian oscillation in the thermocline ridge of the Indian ocean. *Clim Dyn* 37(11–12):2217–2234. doi:10.1007/s00382-010-0953-5
- Joseph S, Wallcraft AJ, Jensen TG, Ravichandran M, Shenoi SSC, Nayak S (2012) Weakening of spring warty jets in the Indian ocean during 2006–2011. *J Geophys Res: Oceans*. doi:10.1029/2011JC007581
- Kara AB, Hurlburt HE, Loh WY (2007) Which near-surface atmospheric variable drives air-sea temperature differences over the global ocean? *J Geophys Res: Oceans*. doi:10.1029/2006JC003833
- Kessler WS (2005) The oceans. In: Intraseasonal variability in the atmosphere–ocean climate system. Springer, pp 175–222
- Krishnamurti TN, Oosterhof D, Mehta A (1988) Air–sea interaction on the time scale of 30 to 50 days. *J Atmos Sci* 45(8):1304–1322
- Kumar BP, Vialard J, Lengaigne M, Murty V, McPhaden M (2012) Tropflux: air–sea fluxes for the global tropical oceans description and evaluation. *Clim Dyn* 38(7–8):1521–1543
- Kumar BP, Vialard J, Lengaigne M, Murty V, McPhaden M, Cronin M, Pinsard F, Reddy KG (2013) Tropflux wind stresses over the tropical oceans: evaluation and comparison with other products. *Clim Dyn* 40(7–8):2049–2071
- Lau WKM, Waliser DE (2012) Intraseasonal variability in the atmosphere–ocean climate system. Springer Science & Business Media. doi:10.1007/978-3-642-13914-7
- Lin JL, Kiladis GN, Mapes BE, Weickmann KM, Sperber KR, Lin W, Wheeler MC, Schubert SD, Del Genio A, Donner LJ et al (2006) Tropical intraseasonal variability in 14 IPCC AR4 climate models. Part I: convective signals. *J Clim* 19(12):2665–2690
- Madden RA, Julian PR (1972) Description of global-scale circulation cells in the tropics with a 40–50 day period. *J Atmos Sci* 29(6):1109–1123
- Madden RA, Julian PR (1994) Observations of the 40–50-day tropical oscillation—a review. *Mon Weather Rev* 122(5):814–837
- Masson S, Delecluse P, Boulanger JP, Menkes C (2002) A model study of the seasonal variability and formation mechanisms of the barrier layer in the eastern equatorial Indian ocean. *J Geophys Res* 107(C12):SRF 18Äçâ, -â€œ1-SRF 18Äçâ, -â€œ20. doi:10.1029/2001jc000832
- Masumoto Y (2005) Intraseasonal variability in the upper layer currents observed in the eastern equatorial Indian ocean. *Geophys Res Lett*. doi:10.1029/2004gl021896
- McPhaden M (1982) Variability in the central Indian ocean. Part I: ocean dynamics. *J Mar Res* 40:157–176
- McPhaden MJ, Meyers G, Ando K, Masumoto Y, Murty VSN, Ravichandran M, Syamsudin F, Vialard J, Yu L, Yu W (2009) Rama: The research moored array for African–Asian–Australian monsoon analysis and prediction*. *Bull Am Meteor Soc* 90(4):459–480. doi:10.1175/2008BAMS2608.1
- Meehl GA (1997) The South Asian monsoon and the tropospheric biennial oscillation. *J Clim* 10(8):1921–1943. doi:10.1175/1520-0442(1997)010<1921:TSAMAT>2.0.CO;2

- Miyama T, McCreary JP Jr, Sengupta D, Senan R (2006) Dynamics of biweekly oscillations in the equatorial Indian ocean*. *J Phys Oceanogr* 36(5):827–846. doi:[10.1175/JPO2897.1](https://doi.org/10.1175/JPO2897.1)
- Nagura M, McPhaden MJ (2008) The dynamics of zonal current variations in the central equatorial Indian ocean. *Geophys Res Lett*. doi:[10.1029/2008gl035961](https://doi.org/10.1029/2008gl035961)
- Rahaman H, Ravichandran M (2013) Evaluation of near-surface air temperature and specific humidity from hybrid global products and their impact on latent heat flux in the north Indian ocean. *J Geophys Res: Oceans* 118(2):1034–1047. doi:[10.1002/jgrc.20085](https://doi.org/10.1002/jgrc.20085)
- Rao R, Kumar MG, Ravichandran M, Rao A, Gopalakrishna V, Thadathil P (2010) Interannual variability of kelvin wave propagation in the wave guides of the equatorial Indian ocean, the coastal Bay of Bengal and the southeastern Arabian sea during 1993–2006. *Deep Sea Res Part I* 57(1):1–13. doi:[10.1016/j.dsr.2009.10.008](https://doi.org/10.1016/j.dsr.2009.10.008)
- Rao SA (2004) Abrupt termination of Indian ocean dipole events in response to intraseasonal disturbances. *Geophys Res Lett*. doi:[10.1029/2004gl020842](https://doi.org/10.1029/2004gl020842)
- Reppin J, Schott FA, Fischer J, Quadfasel D (1999) Equatorial currents and transports in the upper central Indian ocean: annual cycle and interannual variability. *J Geophys Res* 104(C7):15,495–15,514. doi:[10.1029/1999jc900093](https://doi.org/10.1029/1999jc900093)
- Roll HU (1965) *Physics of the marine atmosphere*, vol 7. Academic Press, Cambridge
- Roxy M, Tanimoto Y (2012) Influence of sea surface temperature on the intraseasonal variability of the south China sea summer monsoon. *Clim Dyn* 39(5):1209–1218. doi:[10.1007/s00382-011-1118-x](https://doi.org/10.1007/s00382-011-1118-x)
- Roxy M, Tanimoto Y, Preethi B, Terray P, Krishnan R (2013) Intraseasonal sst-precipitation relationship and its spatial variability over the tropical summer monsoon region. *Clim Dyn* 41(1):45–61. doi:[10.1007/s00382-012-1547-1](https://doi.org/10.1007/s00382-012-1547-1)
- Saji N, Goswami BN, Vinayachandran P, Yamagata T (1999) A dipole mode in the tropical Indian ocean. *Nature* 401(6751):360–363
- Schiller A, Godfrey J (2003) Indian ocean intraseasonal variability in an ocean general circulation model. *J Clim* 16(1):21–39. doi:[10.1175/1520-0442\(2003\)016<0021:IOIVIA>2.0.CO;2](https://doi.org/10.1175/1520-0442(2003)016<0021:IOIVIA>2.0.CO;2)
- Schott FA, McCreary JP (2001) The monsoon circulation of the Indian ocean. *Prog Oceanogr* 51(1):1–123. doi:[10.1016/S0079-6611\(01\)00083-0](https://doi.org/10.1016/S0079-6611(01)00083-0)
- Sengupta D, Ravichandran M (2001) Oscillations of Bay of Bengal sea surface temperature during the 1998 summer monsoon. *Geophys Res Lett* 28(10):2033–2036. doi:[10.1029/2000GL012548](https://doi.org/10.1029/2000GL012548)
- Shankar D, Vinayachandran P, Unnikrishnan A (2002) The monsoon currents in the north Indian ocean. *Prog Oceanogr* 52(1):63–120. doi:[10.1016/S0079-6611\(02\)00024-1](https://doi.org/10.1016/S0079-6611(02)00024-1)
- Shenoi S, Saji P, Almeida A (1999) Near-surface circulation and kinetic energy in the tropical Indian ocean derived from lagrangian drifters. *J Mar Res* 57(6):885–907. doi:[10.1357/002224099321514088](https://doi.org/10.1357/002224099321514088)
- Shetye SR, Gouveia AD (1998) Coastal circulation in the north Indian ocean. Coastal segment (14,S-W) *The Sea Chapter 18*, vol 11. Wiley, pp 523–556
- Shinoda T, Hendon HH (1998) Mixed layer modeling of intraseasonal variability in the tropical western Pacific and Indian oceans. *J Clim* 11(10):2668–2685. doi:[10.1175/1520-0442\(1998\)011<2668:MLM OIV>2.0.CO;2](https://doi.org/10.1175/1520-0442(1998)011<2668:MLM OIV>2.0.CO;2)
- Slingo J, Sperber K, Boyle J, Ceron JP, Dix M, Dugas B, Ebisuzaki W, Fyfe J, Gregory D, Gueremy JF et al (1996) Intraseasonal oscillations in 15 atmospheric general circulation models: results from an amip diagnostic subproject. *Clim Dyn* 12(5):325–357. doi:[10.1007/BF00231106](https://doi.org/10.1007/BF00231106)
- Sprintall J, Tomczak M (1992) Evidence of the barrier layer in the surface layer of the tropics. *J Geophys Res* 97:7305–7316. doi:[10.1029/92JC00407](https://doi.org/10.1029/92JC00407)
- Sura P, Newman M (2008) The impact of rapid wind variability upon air–sea thermal coupling. *J Clim* 21(4):621–637. doi:[10.1175/2007JCLI1708.1](https://doi.org/10.1175/2007JCLI1708.1)
- Trenberth KE, Shea DJ (2005) Relationships between precipitation and surface temperature. *Geophys Res Lett*. doi:[10.1029/2005GL022760.114703](https://doi.org/10.1029/2005GL022760.114703)
- Vialard J, Jayakumar A, Gnanaseelan C, Lengaigne M, Sengupta D, Goswami B (2012) Processes of 30–90 days sea surface temperature variability in the northern Indian ocean during boreal summer. *Clim Dyn* 38(9–10):1901–1916. doi:[10.1007/s00382-011-1015-3](https://doi.org/10.1007/s00382-011-1015-3)
- Waliser DE, Lau K, Kim JH (1999) The influence of coupled sea surface temperatures on the Madden–Julian oscillation: a model perturbation experiment. *J Atmos Sci* 56(3):333–358. doi:[10.1175/1520-0469\(1999\)056<0333:TIOCSS>2.0.CO;2](https://doi.org/10.1175/1520-0469(1999)056<0333:TIOCSS>2.0.CO;2)
- Waliser DE, Murtugudde R, Lucas LE (2003) Indo-pacific ocean response to atmospheric intraseasonal variability: 1. Austral summer and the Madden–Julian oscillation. *J Geophys Res: Oceans* (1978–2012). doi:[10.1029/2002JC001620](https://doi.org/10.1029/2002JC001620)
- Waliser DE, Murtugudde R, Lucas LE (2004) Indo-pacific ocean response to atmospheric intraseasonal variability: 2. Boreal summer and the intraseasonal oscillation. *J Geophys Res: Oceans* (1978–2012). doi:[10.1029/2003JC002002](https://doi.org/10.1029/2003JC002002)
- Webster PJ, Moore AM, Loschnigg JP, Leben RR (1999) Coupled ocean–atmosphere dynamics in the Indian ocean during 1997–1998. *Nature* 401(6751):356–360
- Wheeler M, Kiladis GN (1999) Convectively coupled equatorial waves: analysis of clouds and temperature in the wave-number-frequency domain. *J Atmos Sci* 56(3):374–399. doi:[10.1175/1520-0469\(1999\)056<0374:CCEWAO>2.0.CO;2](https://doi.org/10.1175/1520-0469(1999)056<0374:CCEWAO>2.0.CO;2)
- Wheeler MC, Hendon HH (2004) An all-season real-time multivariate mjo index: development of an index for monitoring and prediction. *Mon Weather Rev* 132(8):1917–1932. doi:[10.1175/1520-0493\(2004\)132<1917:AARMMI>2.0.CO;2](https://doi.org/10.1175/1520-0493(2004)132<1917:AARMMI>2.0.CO;2)
- Wu R, Kirtman BP (2005) Roles of Indian and pacific ocean air–sea coupling in tropical atmospheric variability. *Clim Dyn* 25(2–3):155–170. doi:[10.1007/s00382-005-0003-x](https://doi.org/10.1007/s00382-005-0003-x)
- Wu R, Kirtman BP (2007) Regimes of seasonal air–sea interaction and implications for performance of forced simulations. *Clim Dyn* 29(4):393–410. doi:[10.1007/s00382-007-0246-9](https://doi.org/10.1007/s00382-007-0246-9)
- Wu R, Kirtman BP, Pegion K (2006) Local air–sea relationship in observations and model simulations. *J Clim* 19(19):4914–4932. doi:[10.1175/JCLI3904.1](https://doi.org/10.1175/JCLI3904.1)
- Wyrtki K (1973) An equatorial jet in Indian ocean. *Science* 181:262–264. doi:[10.1126/science.181.4096.262](https://doi.org/10.1126/science.181.4096.262)
- Zhang GJ, Ramanathan V, McPhaden MJ (1995) Convection–evaporation feedback in the equatorial pacific. *J Clim* 8(12):3040–3051. doi:[10.1175/1520-0442\(1995\)008<3040:CEFITE>2.0.CO;2](https://doi.org/10.1175/1520-0442(1995)008<3040:CEFITE>2.0.CO;2)
- Zhang Y, Rossow WB, Stackhouse PW (2006) Comparison of different global information sources used in surface radiative flux calculation: Radiative properties of the near-surface atmosphere. *J Geophys Res*. doi:[10.1029/2005jd006873](https://doi.org/10.1029/2005jd006873)
- Zhang Y, Rossow WB, Stackhouse PW (2007) Comparison of different global information sources used in surface radiative flux calculation: Radiative properties of the surface. *J Geophys Res*. doi:[10.1029/2005jd007008](https://doi.org/10.1029/2005jd007008)